

SGP-TR-193

# **The Significance of CO<sub>2</sub> Solubility in Deep Subsurface Environments**

**Sarah Pistone**

June 2011

Financial support was provided through the  
American Chemical Society,  
and by the Department of Energy Resources Engineering,  
Stanford University



Stanford Geothermal Program  
Interdisciplinary Research in  
Engineering and Earth Sciences  
STANFORD UNIVERSITY  
Stanford, California



## **Abstract**

This paper considers the idea of CO<sub>2</sub> injection into the subsurface with the goal of sequestering carbon dioxide. Sequestration may occur in a couple of ways: in the traditional sense, carbon capture and sequestration would involve direct injection into the ground with the goal of sequestering as much as possible. In addition, the concept of CO<sub>2</sub> sequestration has been modified in within the past ten years to consider circulating CO<sub>2</sub> through the subsurface in order to simultaneously produce heat and sequester CO<sub>2</sub> via fluid loss. To use current terminology, the carbon dioxide would be used as the working fluid in an Engineered Geothermal Systems (EGS). This scenario would have the two-fold advantage of providing renewable electricity generation with simultaneous CO<sub>2</sub> sequestration via subsurface fluid loss. In order to entertain this idea seriously, it is necessary to consider the interactions between CO<sub>2</sub> and the reservoir rock and connate fluid. Laboratory experiments and theoretical work were designed to investigate thermodynamic effects that may occur when solubility is taken into account. A core-scale experiment measured relative permeabilities in the two-phase system, a micromodel experiment qualitatively observed the dynamic dissolution phenomenon, and theoretical analyses put the findings in context and provided a framework to predict results under varied conditions.

The purpose of this research was to analyze and quantify the magnitude of dissolution effects through laboratory and theoretical work. An additional goal was to evaluate the time and length-scales of dissolution and diffusion effects relative to standard hydrodynamic behavior.



## Acknowledgments

First, I would like to acknowledge the American Chemical Society for providing the funding that made this research possible.

Thank you to all the members of the geothermal group who provided friendship and support over the past two years. We had many adventures that I will look back upon fondly. From debaucherous nights in Reno for the GRC annual meeting to beach strolls in Bali for the World Geothermal Congress, we have had some exciting opportunities and hopefully more to come. Rob, as a former member of the group, you were along for many of the adventures and brought me up to speed in laboratory and always encouraged a healthy balance between work and play. Thank you for your help and friendship both inside the lab and out.

Many thanks to Mohammed, Hai, and Kewen who provided many useful tips in the laboratory. Thank you Markus for your generous allowance of time and equipment in the SUPRI-A lab to conduct the micromodel experiments.

To my officemates and dear friends Folake and Irem I owe many thanks to you for your reminders to eat, sleep, and get back to work. Fola we had many late nights together, some of which I don't think I would have made through without you. Irem, you taught me the most important secret to making perfect Turkish coffee and I will miss you.

I am grateful for the support and encouragement that I received from all my friends and family over the past two years. You provided calming advice, an open ear, and tasty food when I was too tired to feed myself.

Finally, thank you Roland for your continuous guidance and support. You granted me many opportunities that would not have been available to me elsewhere, and were patient with me as I slowly evolved from a geologist into an engineer.



# Contents

|   |      |
|---|------|
| Abstract.....                             | v    |
| Acknowledgments.....                      | vii  |
| Contents .....                            | ix   |
| List of Tables .....                      | xi   |
| List of Figures .....                     | xiii |
| 1. Introduction.....                      | 1    |
| 1.1. Problem Statement.....               | 2    |
| 1.2. Report Outline.....                  | 3    |
| 2. Background.....                        | 5    |
| 2.1. Literature Review.....               | 5    |
| 2.1.1. Relative Permeability.....         | 6    |
| 2.1.2. Solubility and Diffusion.....      | 9    |
| 2.2. Active Phase Change .....            | 10   |
| 3. Experimental Studies: Micromodel ..... | 15   |
| 3.1. Experimental Apparatus.....          | 15   |
| 3.2. Experimental Results .....           | 17   |
| 4. Core-Scale Experiment: Methods.....    | 23   |
| 4.1. Core holder Apparatus .....          | 23   |
| 4.2. Methods.....                         | 26   |
| 4.2.1. Preparation .....                  | 26   |
| 4.2.2. Experimental Procedure.....        | 28   |
| 5. Core-Scale Experiment: Results .....   | 35   |
| 5.1. JBN Method.....                      | 35   |
| 5.2. Improvements to System.....          | 39   |
| 6. Theoretical Studies.....               | 41   |
| 6.1. Solubility Model .....               | 41   |
| 6.2. Diffusion Rate Study.....            | 43   |
| 7. Closing .....                          | 47   |
| 7.1. Conclusions.....                     | 47   |
| 7.2. Recommendations for Future Work..... | 48   |
| Nomenclature .....                        | 51   |
| References.....                           | 1    |
| A. Buckley-Leverett Theory .....          | 5    |
| B. LabVIEW Program .....                  | 9    |



## List of Tables

|   |    |
|---|----|
| Table 1 Summary of previous relative permeability experiments. ....               | 7  |
| Table 2 Summary of results from previous relative permeability experiments. ....  | 8  |
| Table 3 Micromodel properties.....  | 15 |
| Table 4 Core properties.....  | 24 |
| Table 5.5 Calculations of residual water saturation based upon mass balance:..... | 36 |
| Table B.1 Configuration for SCXI Chassis .....                                    | 10 |
| Table B.2 Balance model and settings .....  | 10 |



## List of Figures

|  |    |
|--|----|
| Figure 2.1 Active phase change cartoon for immiscible fluids. (a) Two-phase system of water and immiscible gas $P_1=P_2$ . (b) $P_1>P_2$ causes water lamina to advance $R_1<R_2$ (from Stacey, 2008).....   | 10 |
| Figure 2.2 Active phase change cartoon for miscible fluids. (a) Two-phase system of water and $CO_2$ gas $P_1>P_2$ and water lamina would advance, $R_1<R_2$ . (b) $P_1>P_2$ , but now system is in dynamic equilibrium and $CO_2$ would pass through water lamina by chemical gradient (from Stacey, 2008)..... | 11 |
| Figure 2.3 Schematics of multiphase flow with (a) $CO_2$ -water and (b) nitrogen-water (modified from Stacey, 2008). ....  | 12 |
| Figure 2.4 Relative permeability curves for nitrogen (left) and $CO_2$ (right) (Stacey, 2008). ....  | 13 |
| Figure 2.5 Schematic showing reduction in residual water saturation over time. ....  | 13 |
| Figure 3.1 SEM micrograph of Berea sandstone and (left), etched silicon micromodel (right) (from Buchgraber, 2011). ....   | 16 |
| Figure 3.2 Diagram of micromodel in holder (not to scale). ....  | 16 |
| Figure 3.3 Process flow diagram of the micromodel experiment. ....   | 17 |
| Figure 3.4 Approximate locations for reported photomicrographs: (1) Figure 3.5, (2) Figure 3.7, (3) Figure 3.8. ....   | 18 |
| Figure 3.5 2011 micromodel results. Figure 3.6 Stacey (2008) micromodel results.   | 19 |
| Figure 3.7 Dynamic equilibrium in micromodel.....  | 19 |
| Figure 3.8 Bubble dissolution in micromodel.....   | 21 |
| Figure 4.1 Berea sandstone core. ....  | 24 |
| Figure 4.2 Titanium core holder with pressure transducer box (from Stacey, 2008). ....   | 24 |
| Figure 4.3 Schematic of core holder and connections to pressure transducer box. ....   | 25 |
| Figure 4.4 Process flow diagram for core drainage; gas injection (not to scale). ....  | 29 |
| Figure 4.5 Process flow diagram for core imbibition; water injection (not to scale).....   | 29 |
| Figure 4.6 Photos of separator: (a) sealed flask separator with flow transducer, (b) burette separator attached to vacuum pump.....  | 30 |
| Figure 4.7 Calibration curves: transducer 0 shows poor calibration at high pressures, whereas transducer 2 is a very well-behaved transducer. ....   | 31 |

|   |    |
|---|----|
| Figure 4.8 Schematic of injection schedule (from Stacey, 2008). .....   | 32 |
| Figure 5.1 Raw data from transducers. First cycle is OK; all remaining transducers except for Transducer 2 are not.....   | 35 |
| Figure 5.2 “Corrected” pressure data; assumes a constant $dP$ .....   | 36 |
| Figure 5.3 Cumulative gas injection volume; legend applies to Figure 5.6 too.....   | 37 |
| Figure 5.4 Cumulative production curves: (a) Cumulative gas production; solid lines are calculated values and dashed lines were measured values, (b) Cumulative water production. ....                | 37 |
| Figure 5.5 Relative permeability curves for drainage 1, 2, and 3. ....  | 38 |
| Figure 5.6 Residual water saturation over time. ....  | 38 |
| Figure 6.1 (Left) Experimental data versus (Right) Data from thermodynamic model... ..  | 42 |
| Figure 6.2 Schematic of semi-infinite slab diffusion model.....   | 43 |
| Figure 6.3 Diffusion model results: (left) normalized concentration versus distance for lines of constant time, and (right) normalized concentration versus time for lines of constant distance. .... | 44 |
| Figure A.1 Example plot for of $1/(t_D \times I_r)$ vs. $1/t_D$ for Equation A.11.....  | 7  |
| Figure B.1 Example diagram of SCXI connection .....   | 9  |
| Figure B.2 Settings for chassis that transmits voltage data from pressure transducers. ..   | 10 |
| Figure B.3 Front panel of LabVIEW program.....  | 11 |
| Figure B.4 Back Panel of LabVIEW code. ....   | 13 |
| Figure B.5 Front panel of mass data collection program.....   | 14 |
| Figure B.6 Back panel of mass data collection program.....  | 14 |

# Chapter 1

## 1. Introduction

With increasing concern over greenhouse gas (GHG) emissions and global energy security, more research efforts have been directed at renewable energy sources and carbon mitigation strategies. Traditional CO<sub>2</sub> sequestration strategies try to store as much CO<sub>2</sub> underground as possible. An extension to the traditional concept includes Engineered Geothermal Systems (EGS) that could use CO<sub>2</sub> as the working fluid. CO<sub>2</sub> EGS would have the two-fold advantage of providing renewable electricity generation with simultaneous CO<sub>2</sub> sequestration through subsurface fluid loss. CO<sub>2</sub> EGS has not been implemented or field tested to date, but several papers and presentations have been dedicated to this topic at recent conferences and workshops. The chemical kinetics, thermodynamics, and hydrodynamics of a system including CO<sub>2</sub>, reservoir rock, and connate fluids have yet to be fully defined.

The research presented here focused on the multiphase flow behavior CO<sub>2</sub> and water. Specifically, the purpose of this work was to evaluate the effect of CO<sub>2</sub> solubility and diffusion in water on the relative permeabilities of CO<sub>2</sub> and water in rock. Findings indicated that CO<sub>2</sub> solubility in water is very important as it caused residual water saturation to decrease over time. This is suggested to be the result of a phenomenon that was termed “active phase change”, which is apparent only in a soluble gas such as CO<sub>2</sub> and will be explained in more detail later in this report. Results were obtained from laboratory experiments where we considered the simplified case of CO<sub>2</sub> and water (instead of brine) at ambient conditions in order to investigate the phenomenon of active phase change and its effect on apparent relative permeabilities. Continued work in this field should investigate the process at reservoir conditions to see if the predicted results are obtained. Furthermore, procedures should be developed in a way that results are comparable between experiments and between laboratories.

The results of this work may be applied to a variety of fields. Relevant sectors include carbon capture and sequestration (CCS), CO<sub>2</sub> EGS, as well as traditional geothermal systems with natural CO<sub>2</sub> in their reservoir fluids, and enhanced oil recovery (EOR) operations. The most common application of this type of research is to CCS, where there are generally four main mechanisms by which CO<sub>2</sub> may be “trapped” underground: (1) a structural confining layer that acts as a hydrodynamic barrier to flow, (2) mineralization of carbonate species, (3) disconnected gas phase that is immobile due to capillary effects, and (4) solubility trapping where CO<sub>2</sub> dissolves into reservoir fluid, which may be enhanced by gravity effects. “Active phase change” (APC) may serve as a fifth trapping mechanism whereby more CO<sub>2</sub> could be stored than would have otherwise been predicted. Once APC is a proven concept, it may also help operators manage geothermal reservoirs with natural CO<sub>2</sub> in the reservoir fluids. A more complete understanding of the conditions that enhance or degrade CO<sub>2</sub> mobility would help mitigate scaling or corrosion issues. In addition, CO<sub>2</sub> solubility is an important factor in EOR operations that use a water alternating CO<sub>2</sub> gas drive. If the CO<sub>2</sub> dissolves in water in the formation there will be less gas to mix with the residual oil, thus lower total oil production. Perhaps saturating the water with CO<sub>2</sub> prior to injection would help mitigate this problem. Again, and understanding of CO<sub>2</sub> solubility in water and APC may help with the design of more productive EOR schemes.

### **1.1. Problem Statement**

As outlined earlier, the solubility of CO<sub>2</sub> in water is an important mechanism that cannot be ignored when modeling subsurface flow. This has several applications, but this research focused on its relevance CO<sub>2</sub> injection into the deep subsurface. This would be relevant to both traditional concepts of CO<sub>2</sub> sequestration as well as the newer idea of a CO<sub>2</sub> EGS system. It is expected that a development plan designed with APC in mind could help promote an increases storage capacity by removing additional immobile water over time. For CO<sub>2</sub> sequestration this would mean a greater pore volume available to hold CO<sub>2</sub>. For CO<sub>2</sub> EGS, a desired outcome is the so-called reservoir “dry-out” when no more connate fluid would be available to mix with injected CO<sub>2</sub>.

The purpose of this research was to analyze and quantify the magnitude of dissolution effects through laboratory and theoretical work. An additional goal was to evaluate the time and length-scales of solubility and diffusion effects relative to standard hydrodynamic behavior.

## **1.2. Report Outline**

This report is structured as follows:

Chapter 2 Background – Section 2.1 provides a summary of previous literature published on the topics of relative permeability experiments, CO<sub>2</sub> solubility, and CO<sub>2</sub> diffusion in water. In addition, Section 2.2 gives a detailed explanation of active phase change and previous results that help prove this concept in CO<sub>2</sub>-water systems.

Chapter 3 Experimental Studies: Micromodel – This section describes the setup, methods and results, from micromodel experiments. The objective of these experiments was to serve as a visual confirmation of the APC phenomenon and previous results.

Chapter 4 Core-Scale Experiment: Methods – This chapter provides a detailed account of the preparations, apparatus and methodology required to carry out an unsteady-state core flood experiment.

Chapter 5 Core-Scale Experiment: Results – This section shows data from core experiments as well as data analysis. Calculations of relative permeabilities are presented via both the JBN method and history matching.

Chapter 6 Theoretical Studies – Chapter 6 includes a discussion of CO<sub>2</sub> solubility and its relationship with temperature, pressure, and dissolved solids.

Chapter 7 Closing – This final chapter includes conclusions and recommendations for future work.

Finally, there are two appendices attached to this report: Appendix A summarizes equations based on Buckley-Leverett flow theory needed to calculate relative

permeabilities using the JBN method. Also included is a technique to correct for capillary end effects. Appendix B includes a description of LabVIEW and a commented copy of the code used to collect pressure and mass data.

## Chapter 2

### 2. Background

The concept of EGS has been around for several decades, having been first introduced in about 1970 with the Fenton Hill, NM project led by researchers at Los Alamos National Lab, and the concept was later patented by Bob Potter (Potter et al., 1974). Donald Brown modified the basic concept about a decade ago when he introduced the idea of using CO<sub>2</sub> as the working fluid in the EGS reservoir (Brown, 2000). As noted in Chapter 1, there are many uncertainties and data gaps that would need to be filled in before implementing such a design, such as: chemical kinetics of interactions between the rock, reservoir fluid, and CO<sub>2</sub>; multiphase flow of CO<sub>2</sub> and brine in the reservoir; mechanisms of fluid loss; and dry out of the reservoir. EGS is typically envisioned in crystalline rock where permeability is enhanced by purposefully exceeding the principle stresses to fracture the formation and/or induce slip on preexisting faults. Thus, the common conception of EGS is of a reservoir with fracture-dominated flow and a low-permeability matrix. The current research was conducted using porous media, but once the physical behavior of the system is understood, it could be applied to fractured systems too. Furthermore, Randolph and Saar (2010) went so far as to suggest CO<sub>2</sub> EGS in porous media, such as depleted oil and gas reservoirs that have temperatures of 100 °C or more. Nonetheless, the research presented here attempts to address just a component of the problem, namely the multiphase flow behavior of CO<sub>2</sub> and water. This chapter summarizes previous work and concepts as background and is presented in two sections: (2.1) Literature Review and (2.2) Active Phase Change.

#### 2.1. Literature Review

Many papers have been published that address CO<sub>2</sub>-water systems or relative permeability, but not necessarily with the application of CO<sub>2</sub> EGS in mind. This section summarizes previous literature that has been useful in developing laboratory practices and

theoretical analyses; specific subsections include: (2.1.1.) Relative Permeability Literature and (2.1.2.) Solubility and Diffusion Literature.

### ***2.1.1. Relative Permeability***

Typically, two main types of laboratory relative permeability experiments are considered: (1) steady-state and (2) unsteady-state. Bennion and Thomas (1991) provided a succinct analysis of the advantages and disadvantages of both methods, as well as advice on types of relative permeability calculations. Steady-state experiments allow for direct calculation of relative permeabilities at a given saturation, with no special manipulation of data required; the down side is a single experiment may take weeks or months to complete. Unsteady-state experiments are often preferred due to their simplicity and speed, but disadvantages include: capillary end effects, rate-dependent instabilities, and nonequilibrium between fluids. Bennion and Thomas (1991) also describe two main classes of calculations, namely those based on Buckley-Leverett theory (Welge, JBN, and Jones-Roszelle) and simulations that history match experimental data. Buckley-Leverett theory is flawed in that it assumes ideal, Darcy flow behavior, can only be calculated after water breakthrough and it cannot account for capillary pressure, end effects, or heterogeneities.

In contrast, history matching methods use the pressure and production history to predict the relative permeability curves over the entire saturation range, regardless of fractional flow characteristics. The history matching method assumes a functional form of the system that is fit to the data using an iterative, minimum least-square solution scheme. Bennion and Thomas (1991) seemed to prefer this method partly because gravity and capillary pressure effects can be incorporated into the simulation. The authors presented a few different functional forms (exponential, cubic spline, and B-spline) and concluded that the cubic spline and B-spline methods can produce more accurate results than an exponential form, especially when the sample is very heterogeneous or dual-porosity.

Finally, Bennion and Thomas (1991) presented a simple correction technique for endpoint relative permeability values. This includes incrementally increasing the fluid

injection rate after a drainage run and measuring the change in endpoint permeability. If the endpoint permeability stays constant it is safe to assume that capillary effects are negligible. If the endpoint permeability increases or decreases with increasing injection rate then there is a simple correction technique wherein a nonlinear model is fit to the data and relative permeability curves are scaled to fit the corrected endpoint permeabilities. Details of the Buckley-Leverett equations and the end point correction method are included in Appendix A.

Several laboratory projects have been conducted to date that measured relative permeabilities using the methods described. Table 2.1 includes a summary of the types of rock, experimental method, and some settings of the different experiments. Of note is the high variability in sample type, sample properties, and experimental settings. As noted by Müller (2011), these inconsistencies led to variable results that are difficult to compare. Even so, the literature was reviewed and is summarized as follows.

*Table 1 Summary of previous relative permeability experiments.*

| Author                  | Fluids  | Rock Type           | Porosity (%) | Permeability (mD) | Core Size <sup>1</sup> (cm) | Method                   | Pressure (bar) | Temp (°C) | Flow Rate (ml/hr)     |
|-------------------------|---|---------------------|--------------|-------------------|-----------------------------|--------------------------|----------------|-----------|-----------------------|
| Plug and Bruining, 2006 | CO <sub>2</sub> , N <sub>2</sub> , water      | unconsolidated sand | 34 - 38      | 2.00E+05          | not applicable              | Static Pc                | 1, 8, 85       | 21 - 40   | 0.5, 2                |
| Dria et al., 1993       | CO <sub>2</sub> , N <sub>2</sub> , Oil, Brine | dolomite            | 20.2         | 24                | 5 x 45                      | Steady-state and X-ray   | 96.5           | 71        | Not reported          |
| Perrin et al., 2009     | CO <sub>2</sub> , brine                       | Otway sandstone     | 18.2         | 50                | 5.08 x 15.24                | Steady-state and X-ray   | 124            | 50 - 63   | 15, 72, 156           |
|                         |   | Berea sandstone     | 20.3         | 430               |                             |                          |                |           |                       |
| Egermann, 2006          | CO <sub>2</sub> , brine                       | carbonate           | 23 - 23.6    | 4                 | 4.93 x 19.4                 | Unsteady-state and X-ray | 80 - 180       | 60 - 80   | 5, 20, 25, 100        |
| Chalbaud, 2007          | CO <sub>2</sub> , brine                       | carbonate           | 23.6         | 4                 | 4.93 x 11.8                 | Unsteady-State           | 100            | 60        | 5, 25, 100            |
| Bennion and Bachu, 2008 | CO <sub>2</sub> , H <sub>2</sub> S, brine     | sandstone           | 11.7 - 19.5  | 0.081 - 67        | 3.8 x 7.5                   | Unsteady-state           | 90 - 200       | 35 - 75   | Not reported          |
|                         |   | carbonate           | 7.9 - 14.8   | 0.018 - 65        |                             |                          |                |           |                       |
|                         |   | shale               | 3.9 - 4.4    | 2.9E-06 - 7.8E-05 |                             |                          |                |           |                       |
|                         |   | anhydrite           | 1.2          | 3.5E-04           |                             |                          |                |           |                       |
| Stacey, 2008            | CO <sub>2</sub> , N <sub>2</sub> , water      | Berea sandstone     | 23           | 8.9E+02           | 5 x 27                      | Unsteady-state           | 1.2            | 20        | variable <sup>2</sup> |

<sup>1</sup> diameter x length or height depending on if sample is oriented horizontal or vertical.  
<sup>2</sup> total flow rate of injected fluid ranged from 1 - 200 ml/hr or more depending on stage of experiment.

Table 2 Summary of results from previous relative permeability experiments.

| Author                           | Phase           | Krj  | Swj  |
|----------------------------------|-----------------|------|------|
| Dria et al., 1993                | Brine           | 0.36 | 0.36 |
|                                  | Oil             | 0.57 | 0.16 |
|                                  | CO <sub>2</sub> | 0.28 | 0.16 |
| Perrin et al., 2009              | Brine           | 0.5  | 0.9  |
|                                  |                 | 0.5  | 0.95 |
|                                  | CO <sub>2</sub> | 0.6  | 0.44 |
|                                  |                 | 0.1  | 0.57 |
| Chalbaud, 2007<br>Egermann, 2006 | Brine           | 0    | 0.25 |
|                                  | CO <sub>2</sub> | 1    | 0.2  |
| Bennion and<br>Bachu, 2008       | Brine           | 0.27 | 0.75 |
|                                  |                 | 0.9  | 0.9  |
|                                  | CO <sub>2</sub> | 0.07 | 0.48 |
|                                  |                 | 0.54 | 0.29 |

Plug and Buining (2007) performed static capillary pressure experiments at various pressures using unconsolidated sand packs. They used nitrogen as a control to see if CO<sub>2</sub> dissolution had an impact on capillary pressure. They found that at quasistatic conditions diffusion did not play an important role. Another result that was reported in other articles (Chalbaud et al., 2007; Egermann e. al., 2005a, 2005b, and 2006) is that the wettability of water decreases as CO<sub>2</sub> reaches the critical point and the matrix approaches an “intermediate-wet” state.

Dria et al. (1993) and Perrin et al. (2009) both performed steady-state relative permeability experiments. Dria et al. (1993) noticed that N<sub>2</sub> relative permeabilities were an order of magnitude higher than CO<sub>2</sub> relative permeabilities. X-ray was used to identify rock heterogeneities, not to generate saturation profiles. Perrin et al. (2009) used x-rays to monitor heterogeneities and saturation profiles inside the core. They noticed significant heterogeneities perpendicular to flow direction, and that the CO<sub>2</sub> tends to rise to the top side of the core holder.

Chalbaud et al. (2007) and Egermann et al. (2005a, 2005b, 2006) conducted unsteady-state relative permeability experiments on a carbonate core. They found that at higher pressure CO<sub>2</sub> becomes partial-wetting. In addition, Egermann (2005b) included a method to account for localized heterogeneity by calculating local saturation profiles along core.

The method appears to have been successful at matching fluctuating saturations along core and fluctuating pressure (Egermann, 2006).

Bennion and Bachu (2008) conducted core flood experiments and observed greater hysteresis in the CO<sub>2</sub>-brine case than the H<sub>2</sub>S-brine case after primary drainage. Also, the relative permeability of CO<sub>2</sub> was lower than for H<sub>2</sub>S. Based on the lower interfacial tension of H<sub>2</sub>S, Bennion and Bachu would have predicted that CO<sub>2</sub> relative permeability should have been higher and did not have another explanation for the observed phenomena. Their findings were similar to observations in Stacey's core-flood experiments with CO<sub>2</sub>-water and nitrogen-water (Stacey, 2008).

We propose that dynamic dissolution and evolution of CO<sub>2</sub>, or "active phase change", may be responsible for the results of Bennion and Bachu (2008). These effects are described in more detail in Section 2.2.

### ***2.1.2. Solubility and Diffusion***

Some previous studies have produced results that help motivate the relevance of studying CO<sub>2</sub>-water relative permeabilities. Chang et al. (1998) generated a compositional model for CO<sub>2</sub> floods where the CO<sub>2</sub> solubility had a significant impact on ultimate reservoir performance. During simulation of water-alternating-gas (WAG) floods, it was found that when CO<sub>2</sub> solubility in water was taken into account up to 10% of the CO<sub>2</sub> dissolved in the water, which delayed total oil production. Other factors such as salinity or dissolved solids also reduced CO<sub>2</sub> solubility. In addition, Duan et al. (2003, 2006) generated a solubility model that calculated CO<sub>2</sub> solubility as a function of temperature (0 – 260 °C), pressure (0 – 2000 bar) and salinity (0 – 4.5 molality salts). Their model matched the behavior of previous experimental data.

Tamimi et al. (1994) measured liquid phase diffusion coefficients for CO<sub>2</sub> at temperatures 0-95 °C using a wetted sphere.

Xu et al. (2002) measured tracer diffusion coefficients for water in liquid and supercritical CO<sub>2</sub> as a function of temperature (10-35°C) and pressure (130-300 bar) using pulsed field gradient nuclear magnetic resonance (NMR).

Medvedev et al. (2003) presented a method to check the agreement between experimental diffusion coefficients and equations of state.

## 2.2. Active Phase Change

The concept of “active phase change” (APC) was first presented by Chen (2005) during investigation of fundamental flow characteristics in steam-water systems. To illustrate this concept, first consider a system with two immiscible fluids, such as nitrogen gas and liquid water, with a single water lamina in a pinched capillary tube (Figure 2.1.a). If a pressure were to be applied to the left-hand side, the lamina would advance slightly downstream (Figure 2.1.b). This would be an example where no APC would be expected and flow behavior would simply be a function of capillary pressure. Next, consider a two-phase, single component system of steam and water with the same water lamina in a pinched capillary tube with steam on either side. If the upstream pressure were increased a small amount of volume of steam would be expected to condense on the upstream side and a small amount of water would then be expected to evaporate on the lower-pressure (downstream) side. As such, it would appear that the steam traveled through the water lamina, but in actuality it would have been a consequence of the thermodynamic effect that was termed "active phase change" by Chen (2005).

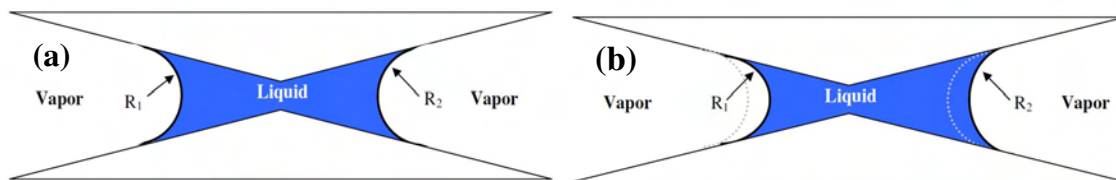


Figure 2.1 Active phase change cartoon for immiscible fluids. (a) Two-phase system of water and immiscible gas  $P_1=P_2$ . (b)  $P_1>P_2$  causes water lamina to advance  $R_1<R_2$  (from Stacey, 2008).

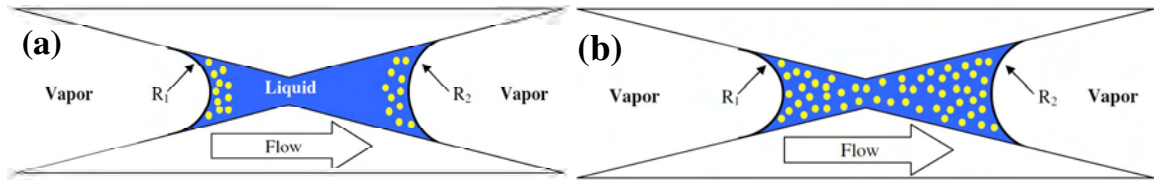


Figure 2.2 Active phase change cartoon for miscible fluids. (a) Two-phase system of water and CO<sub>2</sub> gas  $P_1 > P_2$  and water lamina would advance,  $R_1 < R_2$ . (b)  $P_1 > P_2$ , but now system is in dynamic equilibrium and CO<sub>2</sub> would pass through water lamina by chemical gradient (from Stacey, 2008).

This theory was extended to the context of a two component system of miscible fluids, such as gaseous CO<sub>2</sub> and liquid water, by Stacey (2008). Consider a similar configuration to the two previous examples with a water lamina in a pinched capillary tube with CO<sub>2</sub> gas on either side (Figure 2.2.a). In a CO<sub>2</sub>-water system a phenomenon analogous to APC in the steam-water system is likely to occur. However, instead of steam-water system where the fluid would condense and evaporate through the water lamina; the CO<sub>2</sub>, owing to its solubility in water, would be expected to dissolve on the higher-pressure (upstream) side, and evolve out of solution on the lower-pressure (downstream) side (Figure 2.2.b). Thus the condensation and vaporization in the steam-water case are replaced by dissolution and evolution in the CO<sub>2</sub>-water case. Chemical diffusion is a much slower physical process than water advection, however at the pore scale a pore throat may be on the order of 100  $\mu\text{m}$ , so the process may not be neglected.

The significance of the APC behavior is that it is possible for CO<sub>2</sub> to flow in a disconnected phase in front of the main CO<sub>2</sub> front (Figure 2.3.a). This occurs because of a supersaturated zone where it is possible for bubbles to nucleate contribute to flow. This would not be the case with an insoluble gas such as nitrogen, where the immiscible gas could only flow via hydrodynamic forces and a pore throat may only be entered once the capillary entry pressure has been exceeded (Figure 2.3.b).

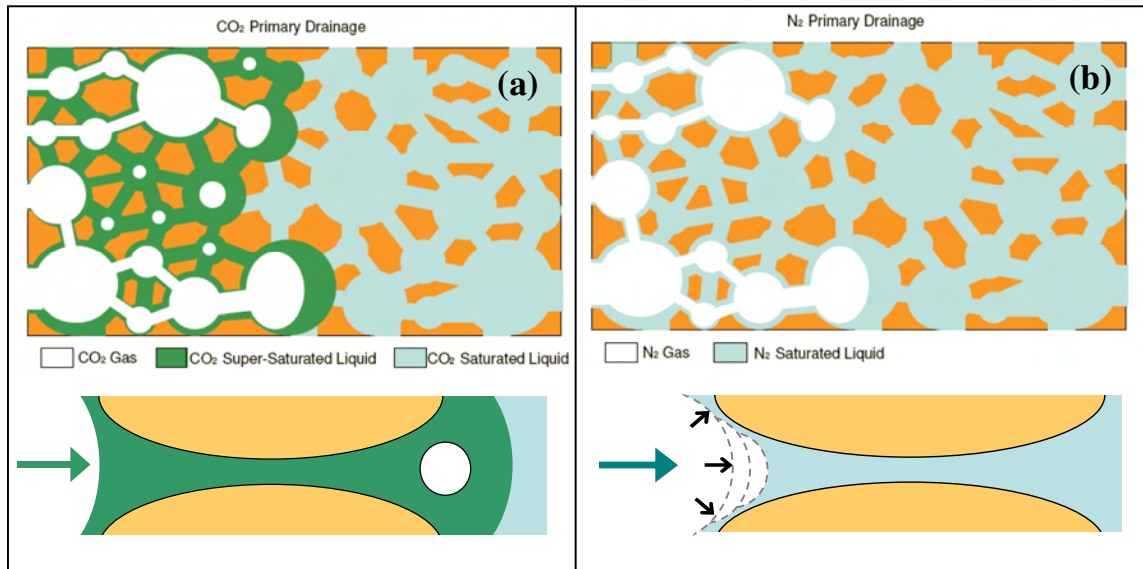


Figure 2.3 Schematics of multiphase flow with (a) CO<sub>2</sub>-water and (b) nitrogen-water (modified from Stacey, 2008).

Previous results show that for nitrogen after primary drainage, the residual water saturation stays approximately constant with continued cycles of drainage and imbibition (Figure 2.4). For CO<sub>2</sub>, a gas highly soluble in water, the residual water saturation decreases with every cycle of drainage and imbibition (Figure 2.4, Stacey, 2008). This is believed to be another significant effect of APC. The conceptual model of how the residual water saturation decreases over time is illustrated in Figure 2.5: first CO<sub>2</sub> may enter the smallest pore spaces via dissolution and diffusion without ever overcoming the capillary entry pressure, after drainage when CO<sub>2</sub> evolves out of solution it displaces some water that was previously immobile into higher-permeability pathways. In this way, immobile water is made mobile and the residual water saturation may decline over time with increasing cycles of drainage and imbibition. Furthermore, the additional mobile water also impedes the flow of CO<sub>2</sub>, thus the relative permeability of CO<sub>2</sub> is less than nitrogen.

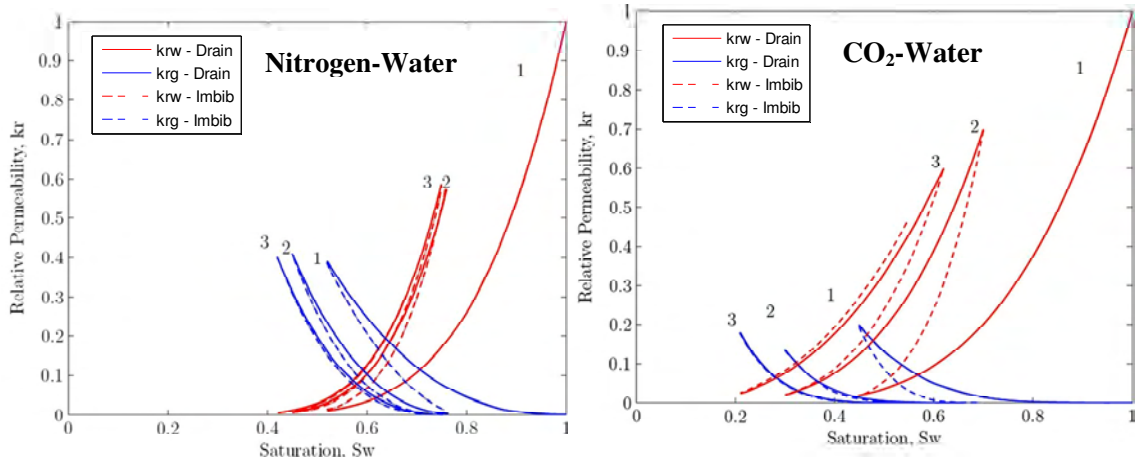


Figure 2.4 Relative permeability curves for nitrogen (left) and CO<sub>2</sub> (right) (Stacey, 2008).

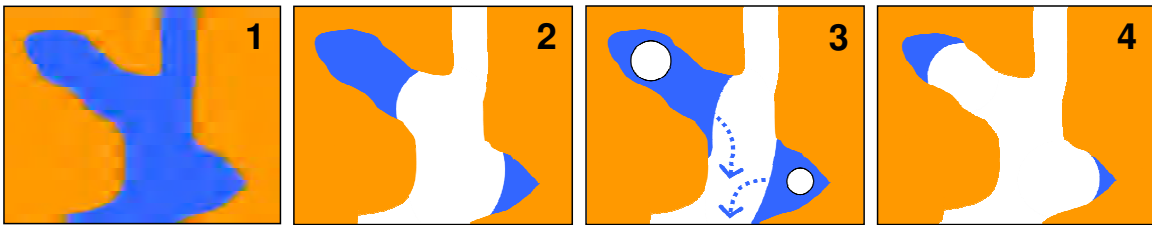


Figure 2.5 Schematic showing reduction in residual water saturation over time.



# Chapter 3

## 3. Experimental Studies: Micromodel

Experimental studies for this research were divided into two main sections: micromodel experiments (Chapter 3) and core flooding experiments (Chapter 4). The micromodels are intended to be a qualitative check on two-phase flow behavior of CO<sub>2</sub> and water, and to observe the phenomenon of APC visually. The core flood experiments are a method to measure relative permeabilities quantitatively and evaluate the significance of CO<sub>2</sub> solubility and APC. The two experiment sets complement each other in providing insight into the physical flow behavior of a CO<sub>2</sub>-water system.

### 3.1. Experimental Apparatus

A micromodel experiment was designed to observe the phenomenon of APC qualitatively. A silicon micromodel fabricated at the Stanford Nanofabrication Facility and was etched to mimic the pore structure of a Berea sandstone (Figure 3.1). The micromodel has an etched depth of 25 μm comparable to the width of a single pore throat, so the micromodel is envisaged as a two-dimensional model of the pore space. Physical properties of the micromodel are listed in Table 3.1. The micromodel experiment was intended to mimic the core experiment as closely as possible. The micromodel was etched to resemble the pore structure of a Berea sandstone (e.g. size, porosity, permeability), which is the rock type used in the core floods.

*Table 3 Micromodel properties*

| Micromodel Properties |          |    |
|-----------------------|----------|----|
| dimensions            | 5 x 5    | cm |
| grain size            | 30 - 200 | μm |
| permeability          | 500      | mD |
| porosity              | 0.20     |    |

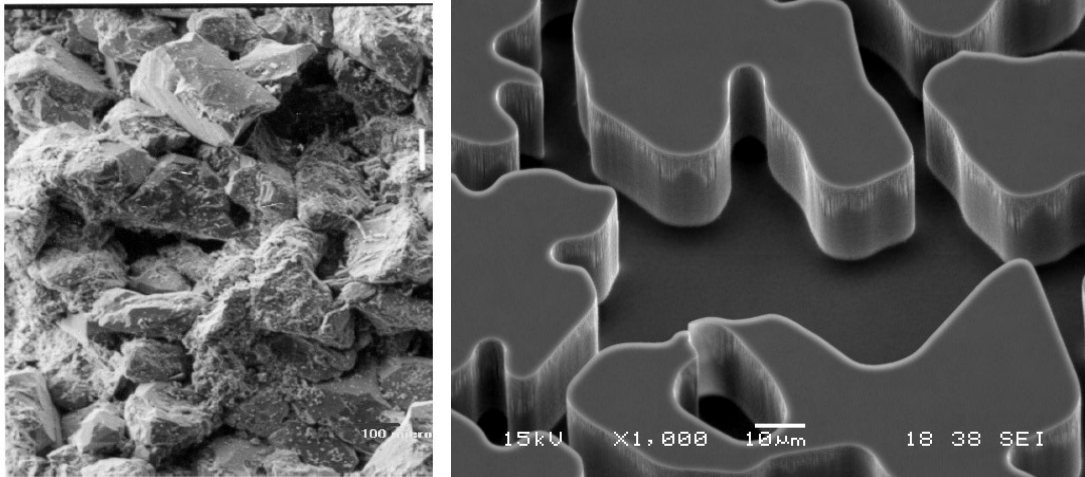


Figure 3.1 SEM micrograph of Berea sandstone and (left), etched silicon micromodel (right) (from Buchgraber, 2011).

These experiments act as a window through the core holder and the hope is that we are observing behavior analogous to flow through the three-dimensional core that would otherwise be obscured from view. The model is etched so that there is a channel along the inlet and outlet edges to maintain a constant pressure boundary (Figure 3.2). The model is sealed inside a holder with a port at each corner of the micromodel. CO<sub>2</sub> is fed from a gas canister to the inlet side while the other inlet port is capped and the two outlet ports are open to the atmosphere. A process flow diagram of the micromodel setup is included in Figure 3.3.

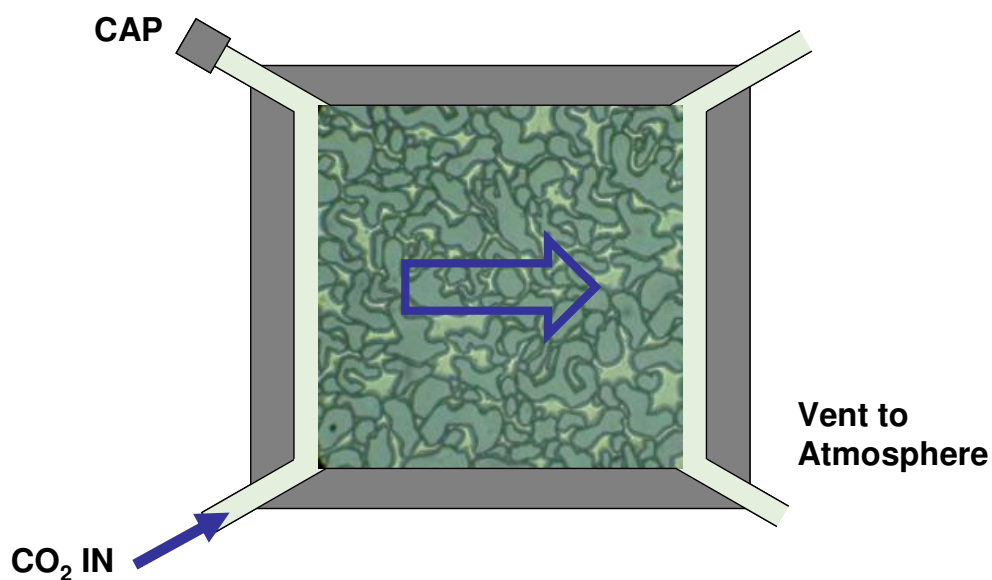


Figure 3.2 Diagram of micromodel in holder (not to scale).

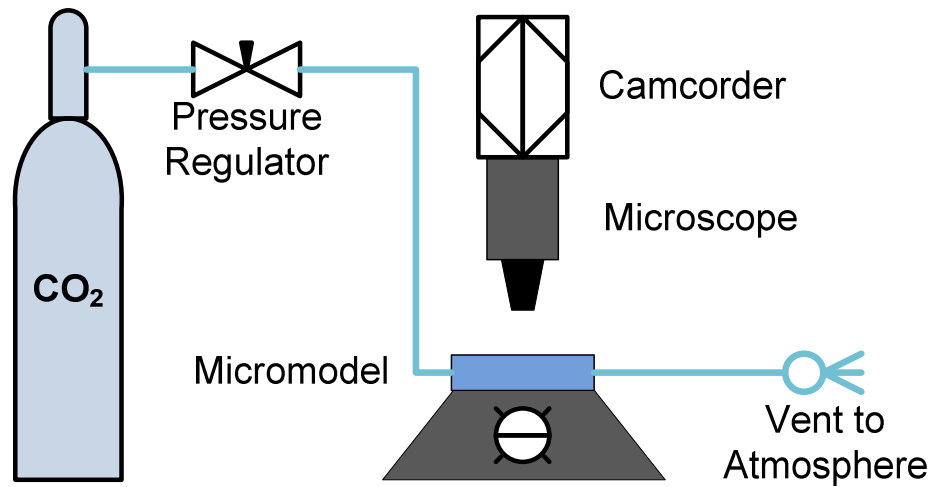


Figure 3.3 Process flow diagram of the micromodel experiment.

The methodology of the experiments is as follows:

First, the micromodel is saturated with distilled water by pumping water into the model at a low flow rate for about 10 minutes. Often the outlet side of the model will not be fully saturated, but this is not a problem, because observations focused on the inlet and middle portion of the model. If needed, full saturation could be achieved by pulling a vacuum on the model prior to saturation.

Next, the CO<sub>2</sub> line was attached to the micromodel. It was helpful to cap the end of the CO<sub>2</sub> line to adjust the pressure regulator to obtain a steady inlet pressure prior to attaching the line to the inlet port. Otherwise, if the valve was accidentally opened too much and model would drain prematurely. We wanted to observe dissolution effects so the inlet pressure was set to 2 psig, which was well below the capillary entry pressure of about 8 psi. Once the steady inlet pressure was achieved, the CO<sub>2</sub> line was attached to the inlet port without touching the pressure regulator. Finally, the microscope was focused on the pore space and the camcorder was started.

### 3.2. Experimental Results

Observations were focused on the inlet portion of the model where the CO<sub>2</sub> front was visible in the constant pressure channel abutting the etched pore network. In addition, the

outlet portion of the model was avoided for observations since it was not fully saturated with water. The first signs that CO<sub>2</sub> gas entered the pore space occurred in the center of the micromodel on the inlet interface. CO<sub>2</sub> flow phenomena observed included disconnected bubbles, advancing gas clusters, and bubble dissolution. To orient the reader and help with future experiments an approximate location map of later images is included (Figure 3.4).

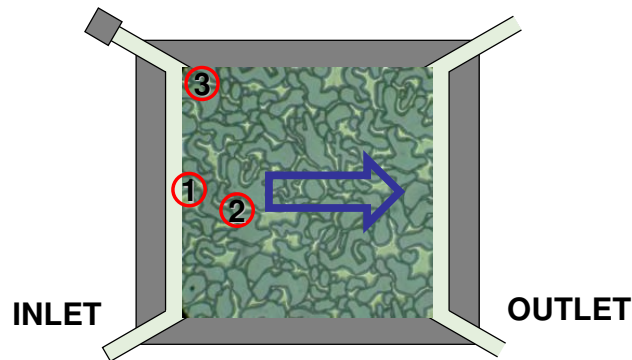


Figure 3.4 Approximate locations for reported photomicrographs: (1) Figure 3.5, (2) Figure 3.7, (3) Figure 3.8.

The first bubbles were observed within the pore space after about 20 min. Figures 3.5 and 3.6 show that the results are similar to previous observations by Stacey (2008). In Figure 3.5 the CO<sub>2</sub> front is visible on the left side of each frame where it abuts the edge of the pore network. In one location (identified by red arrow) the interface is advancing and retreating into a pore throat. At the same time, the bubbles within the pore space change size and shape with each time step. Similarly, in Stacey's images (Figure 3.6) the bubbles are shown to grow, shrink, nucleate and dissolve with each time step. The direction of CO<sub>2</sub> flow was from left to right in all micromodel images (Figures 3.5 – 3.8). The current results show a similar behavior to previous results, but were not quite as dramatic. It would be useful to repeat the experiment replacing the distilled water used to saturate the model with carbonated water, as these may have been the conditions under which the previous experiment was run. Under such conditions bubbles would nucleate much more readily because much less CO<sub>2</sub> gas would need to dissolve to supersaturate the water in the pore space.

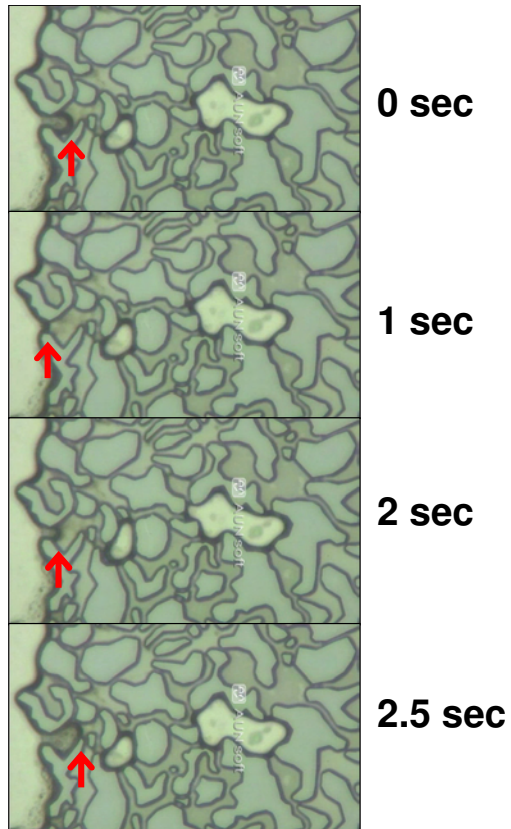


Figure 3.5 2011 micromodel results.

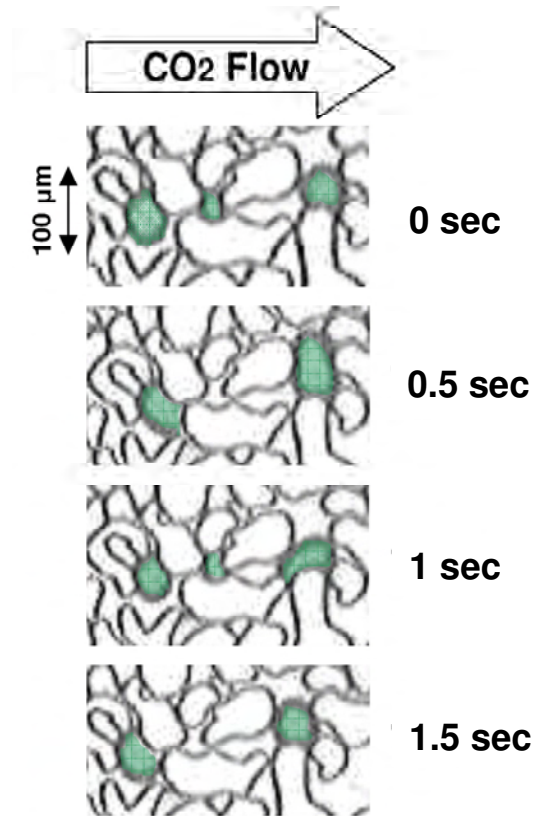


Figure 3.6 Stacey (2008) micromodel results.

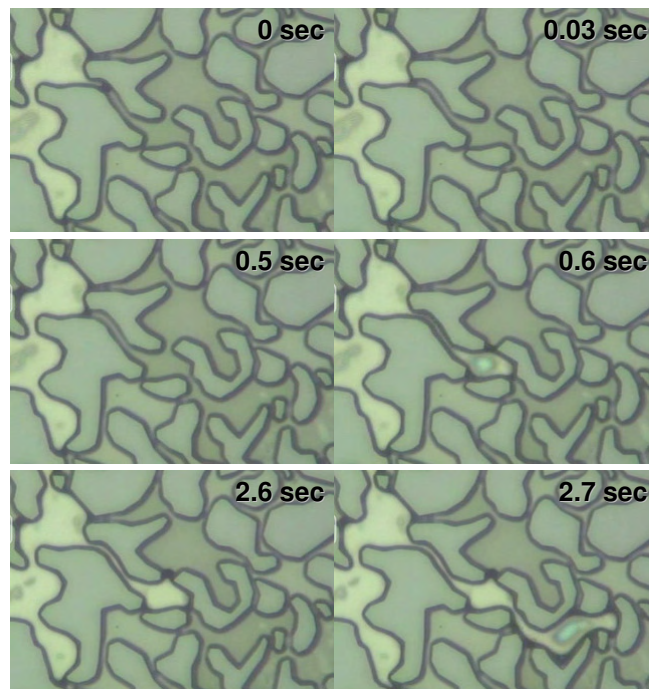


Figure 3.7 Dynamic equilibrium in micromodel.

Another distinct observation was that the CO<sub>2</sub> front seems to remain in a period of stasis interrupted by a rapid advancement that occurs within a fraction of a second (Figure 3.7). This behavior agrees with observations that were noted in previous micromodel studies (Li and Yortsos, 1995 and Tsimpanogiannis and Yortsos 2002). Their studies differed in that they saturated their micromodel with supersaturated carbonated water at moderate pressure (about 56 psi) and then lowered the pressure at a constant rate to observe bubble nucleation and growth. In their scenario there was no flow through the cell, just a static pressure decline. Nonetheless, what they observed was that the growth of a gas cluster occurred in two steps: (1) a slow pressurization step where the volume remains approximately constant and the curvature of the gas-liquid interface changes only slightly to adjust to the pore geometry, followed by (2) a fast penetration step (that can be approximated as a volume increase at constant pressure) after the capillary entry pressure at a perimeter pore throat has been exceeded (Li and Yortsos, 1995). Furthermore, they noted that only one perimeter pore throat was invaded at a time and that all interfaces at the edges of the cluster would adjust after the sudden volume increase.

Even though our experimental configuration was quite different a similar behavior was noted later in the micromodel experiment (Figure 3.7). In the first set of frames you can see a small adjustment that occurs at the edge of the interface such as would be expected in the first step that Li and Yortsos describe. In the second and third sets of frames you can see a sudden (<0.1 sec) gas volume increase after a new pore throat was invaded. Between each set of frames was a period of negligible change. You may notice a slight light refraction on some of the invading CO<sub>2</sub> gas; the micromodel was contaminated with a small amount of light oil. It is not clear if the oil contamination affected flow behavior.

Bubble dissolution was observed in the micromodel too. Figure 3.8 shows a series of frames recorded about 3 hours into the experiment. The location on the micromodel was near the edge of the inlet side of the model. In the following frames you can see bubble shrinkage and dissolution, which clearly show that mass transfer occurred within the pore space.

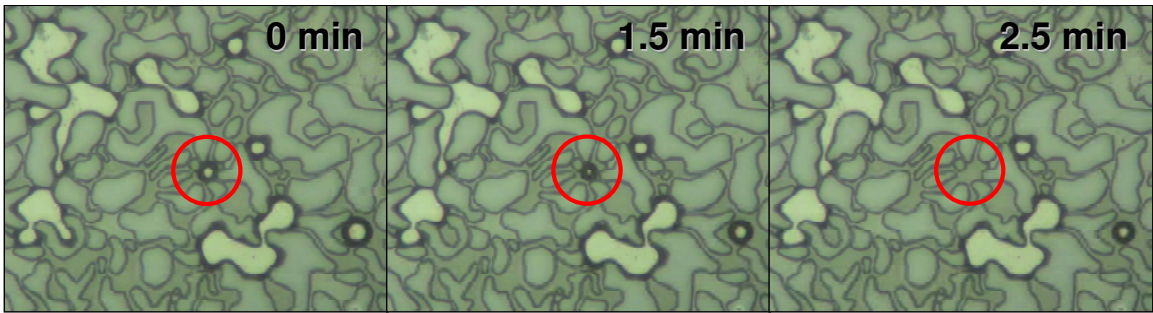


Figure 3.8 Bubble dissolution in micromodel.

At this point, only drainage experiments have been conducted in the micromodel to observe the disconnected flow of  $\text{CO}_2$  as a result of dissolution mass transfer through the water. Later, it may be insightful to continue consecutive imbibition and drainage cycles to see if the conceptual model of APC (Section 2.2) can be verified visually.



# Chapter 4

## 4. Core-Scale Experiment: Methods

### 4.1. Core holder Apparatus

Similar core flood experiments were previously conducted by Rob Stacey in 2008 as mentioned in Chapter 2. My efforts were focused on demonstrating repeatability of these experiments as well as clear documentation the methods utilized to collect the desired data. In this case, the desired data were pressure along the core, total gas injection, total water production, and total gas production. These data were sufficient to maintain a mass balance across the core from which saturations and relative permeabilities could be calculated.

The core used was a Berea sandstone fit into a titanium core holder. On either end of the core was a metal spacer to hold the core in place, which had machined grooves to distribute flow evenly across core ends. Around the entire body of the core was a rubber sleeve upon which a confining pressure was applied. A photograph of the titanium core holder attached to transducer box is included in Figure 4.2. The same Berea sandstone core (Figure 4.1) was used in the current work as the one used in previous relative permeability core experiments (Stacey, 2008). Specific core properties are included in Table 4.1. Berea sandstone is often used in laboratory experiments because it has relatively consistent material properties. It is comprised of quartz grains bonded by silica and minimal clay content (about 1 %), generally with a high porosity and permeability ([www.bereasandstonecores.com](http://www.bereasandstonecores.com)). The core flood experiments were attempted using water and either CO<sub>2</sub> or N<sub>2</sub>. Nitrogen was used as the control for the experiment because its solubility in water is very low.

There were a total of 16 pressure transducers, but only 12 could be used at any one time. Four gauge pressures could be measured using either a high-pressure (100 psi) gauge or a

low-pressure (10 psi) gauge. The remaining eight transducers measured differential pressures along the core (Figure 4.3). The pressure transducers sent a voltage signal that was read and recorded on the computer using LabVIEW; details of the LabVIEW program are included in Appendix B.

Table 4 Core properties

| Core Properties |                  |        |                 |
|-----------------|------------------|--------|-----------------|
| d               | diameter         | 5.089  | cm              |
| L               | length           | 27     | cm              |
| k               | permeability     | 885    | mD              |
| V               | core volume      | 549.2  | cm <sup>3</sup> |
| V <sub>p</sub>  | pore volume      | 128.5  | cm <sup>3</sup> |
| φ               | porosity         | 0.23   |                 |
| m <sub>d</sub>  | dry weight       | 1087.7 | g               |
| m <sub>s</sub>  | saturated weight | 1216.2 | g               |



Figure 4.1 Berea sandstone core.

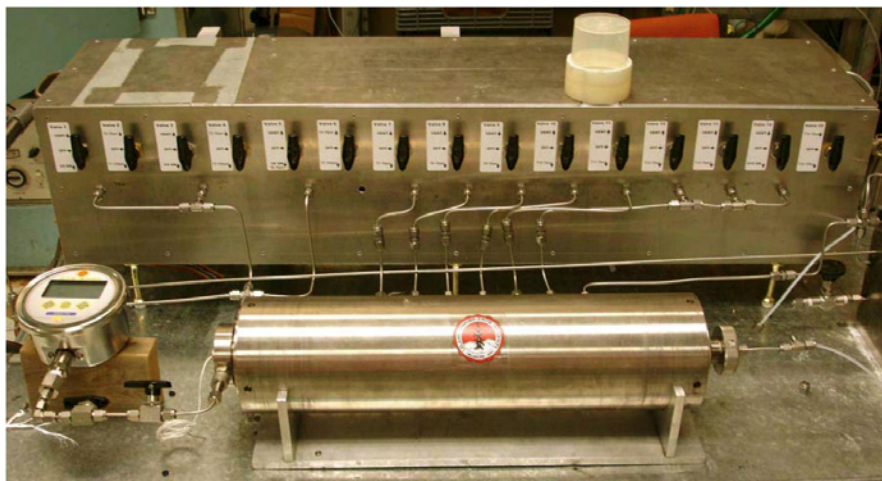


Figure 4.2 Titanium core holder with pressure transducer box (from Stacey, 2008).

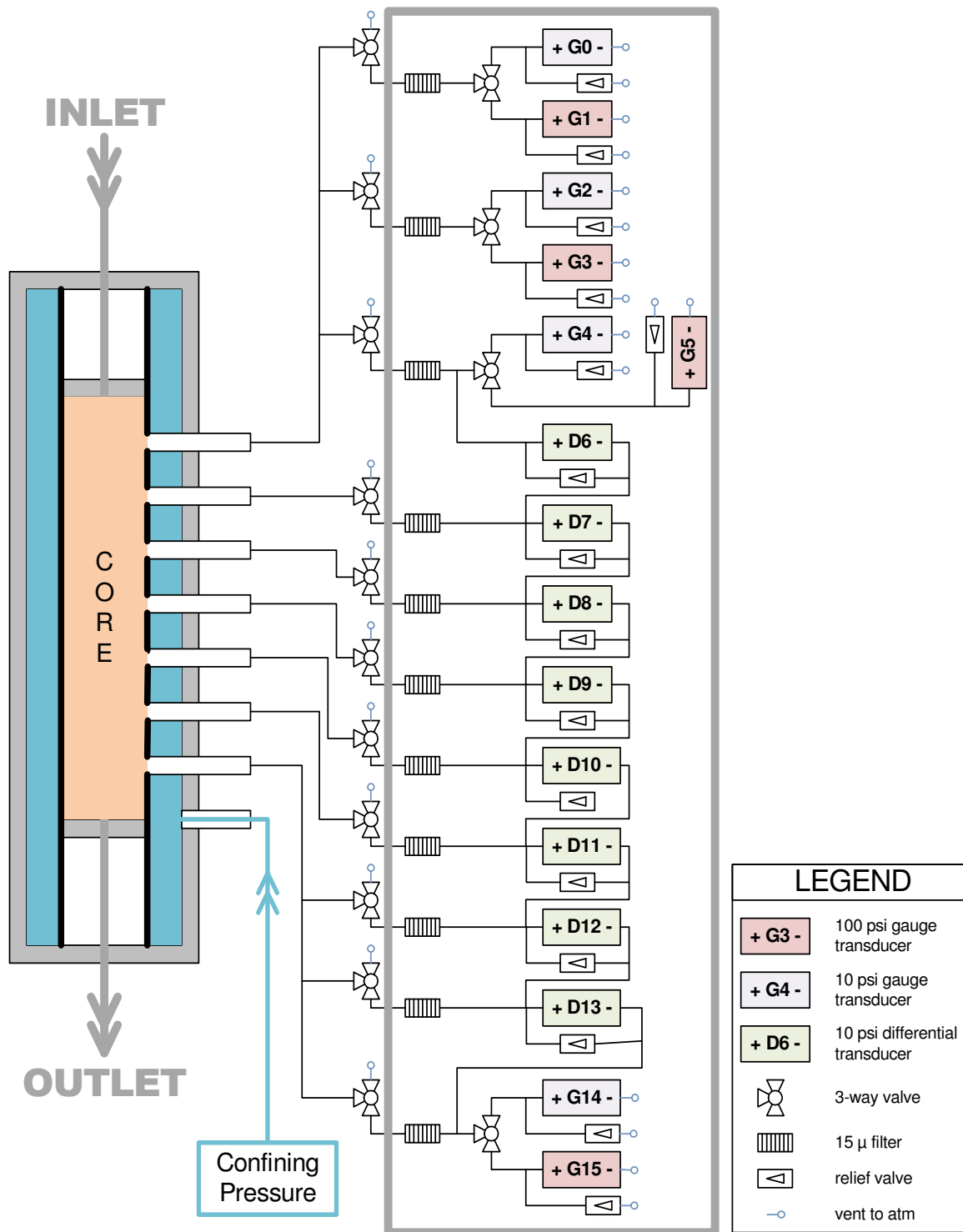


Figure 4.3 Schematic of core holder and connections to pressure transducer box.

## **4.2. Methods**

Preparing the system to run an experiment was a very involved process. Previous works did not explain system preparation in great detail, which led to many pitfalls during laboratory work. It was time-consuming to understanding the system, set it up, learn LabVIEW and write the necessary programs to process the data. Section 4.2.1 is included to provide extra details regarding laboratory methods that were not recorded previously. Additionally, Appendix B explains how the LabVIEW program collects data from the transducers and includes the commented code. Hopefully, the following sections will provide future researchers with the time-saving information to configure a similar project or move the existing one forward. Furthermore, there are improvements that could be made that will be addressed in Section 4.2.4. Therefore, the details ensure the reader knows exactly what was done so adjustments may be made to meet future research objectives. This section helps meet one goal of this report, which was to establish a consistent and repeatable method of performing these unsteady-state relative permeability displacement experiments.

### ***4.2.1. Preparation***

The core was dried in an oven at 200°C for about 2 hours. Originally this was to deactivate clays so that they would not swell when water was introduced, this time it was just to dry the core and confirm the dry weight reported by Stacey (2008) (Table 4.1).

After drying the core, it was fitted back into the core holder inside the rubber sleeve and sealed in. The next few steps included: apply confining pressure, vacuum core, and saturate core. Before introducing fluid to the core chamber, water was pumped into the annulus outside the rubber sleeve up to the desired confining pressure (400 psi). Then, to prepare for saturating the core, a vessel of distilled water was vacuumed to remove

dissolved gas for about 1 hr. If deaeration was done in a transparent container, than it was possible to watch the dissolved gas come out of solution<sup>1</sup>.

In order to saturate the core with the deaerated water, it must first be vacuumed to remove any air and to draw the water into the system. The entire system must be deaerated and saturated with water including the transducers. As the transducers may be damaged if pressurized unevenly, two procedures were tried to saturate the transducers:

1. Close all the valves along the front of the transducer box so that the transducers are never vacuumed. First, vacuum and saturate the core and lines leading up to valves. Then pressurize core and bleed the air from lines behind valves by opening the bleed screws on each transducer one at a time.
2. Attach tubing to the back of gauge transducers that are open to atmosphere (e.g. 0, 1, 2, 3, 4, 5, 14, and 15) and tie the lines in with the rest of the system so that the vacuum pulls evenly on both sides of the transducer. Then the whole system will be saturated together.

Method 1 was very time-consuming and nearly impossible to complete properly. The Allen screws to the bleed transducer diaphragms are stripped on some units making loosening and tightening problematic. Furthermore, the clearance below the transducer box to access the transducers is very tight. Given the difficulties of Method 1, Method 2 was tried as it bypasses the need to touch the Allen screws except to find leaks. Recall that the system can only access one transducer from the 10 psi gauge and 100 psi gauge pair at a time, so there would be a total of four transducers to tie into the vacuum at a time. For these experiments I used only the low pressure set (0, 2, 4, and 14) (see Figure 4.3). Method 2 was also a good way to ensure that the bleed screws were closed properly.

---

<sup>1</sup> Before each use of the vacuum pump the glass vacuum trap was emptied of water and the bucket was filled with dry ice. If the vacuum pump oil were to be contaminated with water the acidity would increase and corrode the pumps internal parts. If water should reach the pump housing then the oil should be changed.

If there was a small leak from a bleed screw it would prevent a vacuum of the system from being achieved.

The system was configured with the deaerated water at the outlet and the vacuum on the inlet side of the core holder. Typically, the vacuum pump would be left on for 10 – 15 minutes to evacuate the trap and tubes and to check pump connections. Then, the needle valve to the core holder system was opened slowly. If the pressure did not drop then the system was checked for leaks<sup>1</sup>. After the core holder and system pressure dropped sufficiently (generally less than 100 millitorr), the pump was left running for about 3 hours to make sure the vacuum held. Then, to saturate the system, the valve to the pump was closed and the valve to the deaerated water vessel was opened<sup>2</sup> so that water would flow from the water vessel through the core and transducer system. The core system was allowed to sit overnight to equilibrate (~ 12 hrs).

#### ***4.2.2. Experimental Procedure***

After the system was prepared and the core was saturated as detailed in Section 4.2.1, the configuration was modified to the format necessary for the drainage and imbibition experiments (Figure 4.4 and Figure 4.5). The setup for the displacement experiment would be identical regardless of which gas (CO<sub>2</sub> or N<sub>2</sub>) was used. Inside a steel canister water was first deaerated with the vacuum pump and then saturated with the respective gas (CO<sub>2</sub> or N<sub>2</sub>). The gas-saturated gas was then used to displace the deaerated water in the core (as in Figure 4.5) by injecting at least one pore volume plus some extra to account for tubing volume (about 175-200 ml seemed sufficient).

---

<sup>1</sup> The first time, it was helpful to use shop air and Snoop to check connections before switching over to vacuum.

<sup>2</sup> After the water was deaerated, the pressure was released in the water vessel to atmospheric immediately before opening the valve to saturate the core.

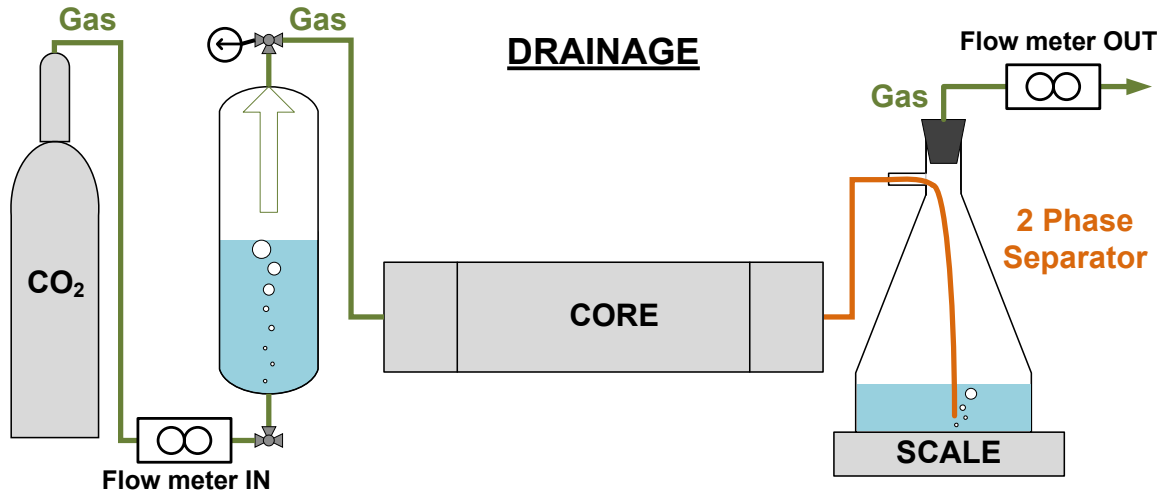


Figure 4.4 Process flow diagram for core drainage; gas injection (not to scale).

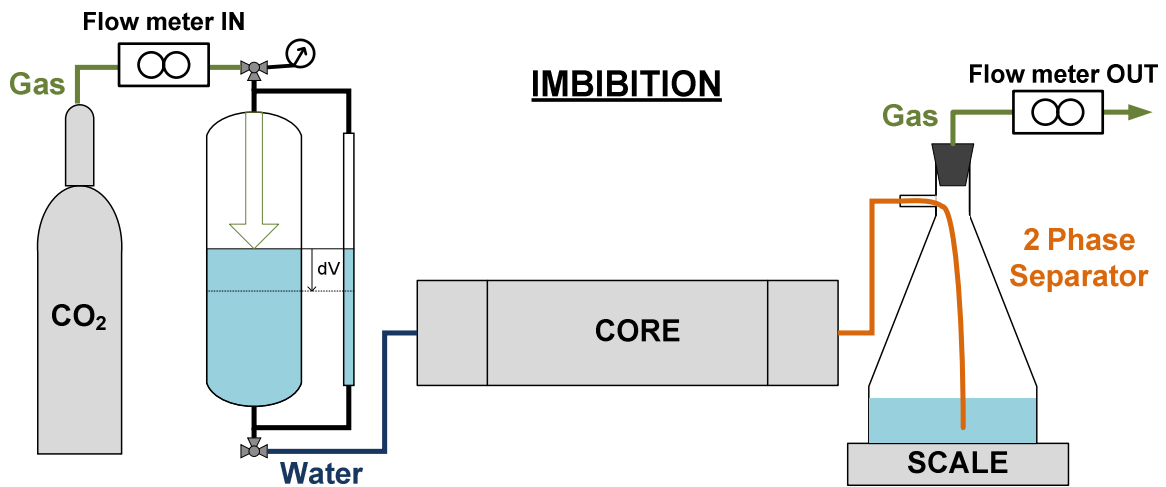


Figure 4.5 Process flow diagram for core imbibition; water injection (not to scale).

The general system configuration consisted of an inlet flow of single-phase fluid and an outlet flow of two-phase fluid. For inlet of the drainage experiment the dry  $\text{CO}_2$  from the tank was bubbled into a canister  $\frac{1}{2}$ -filled with  $\text{CO}_2$ -saturated water to at least partially equilibrate the gas with the water. For the imbibition experiment the dry  $\text{CO}_2$  was injected into a canister filled with  $\text{CO}_2$ -saturated water. In both cases the flow rate into the canister was recorded with readings from a mass flow transducer and the pressure inside the canister was monitored with a manual pressure gauge. For imbibition, the total volume of water injected could also be calculated from the change in liquid level, which was calibrated by filling the vessel from a graduated cylinder ( $7.1 \text{ ml/mm} \pm 0.05 \text{ ml}$ ).

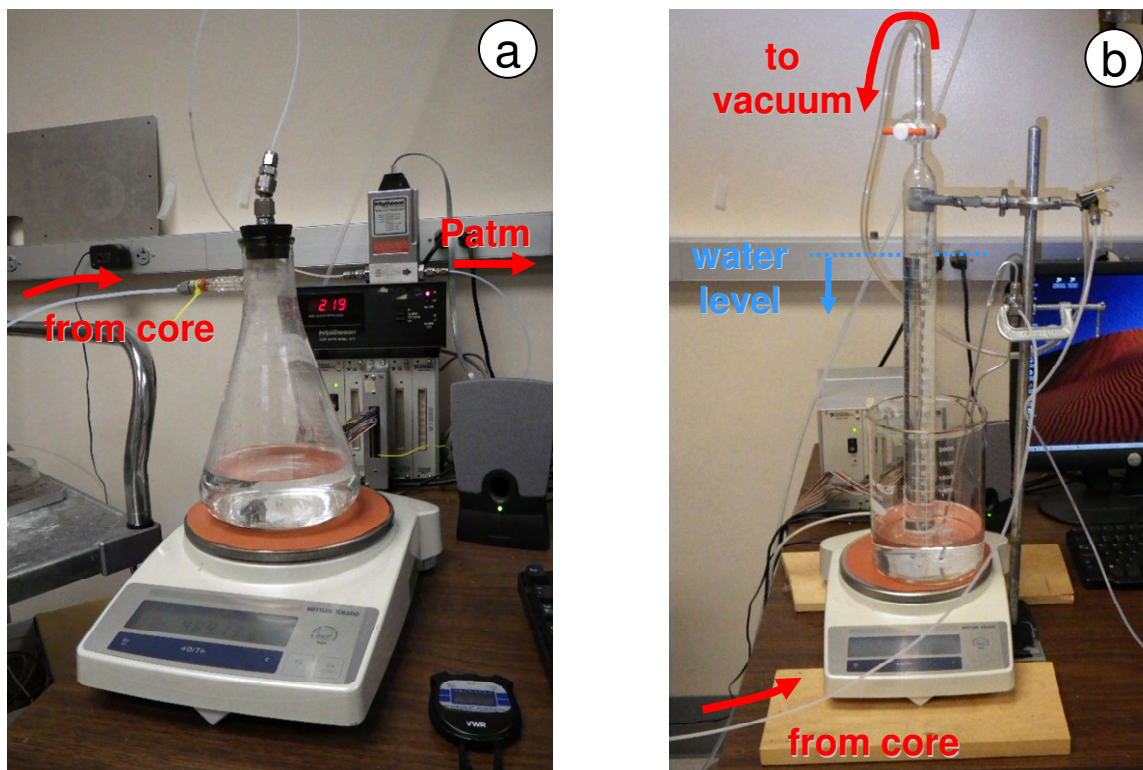


Figure 4.6 Photos of separator: (a) sealed flask separator with flow transducer, (b) burette separator attached to vacuum pump.

At the outlet of the core holder the two-phase fluid stream was directed into a gas, liquid separator; two options were considered for the separator: (a) a sealed Erlenmeyer flask and (b) an inverted burette (Figure 4.6). The Erlenmeyer flask was used as the separator to collect the data reported later in this chapter. Method (a) had the benefit data of digital readings from the outlet mass flow transducer; however the resolution of these data can be quite low especially at low flow rates. Option (b) used an inverted burette submerged in a beaker of water. The vacuum pump was attached to the top end of the burette and the valve could be opened to pull the water vertically into the burette. A thin aluminum tube was bent to direct the two-phase outlet flow inside the burette, which acted as the separator, as the gas came out of solution the water level would be forced lower in the tube. The advantage of this system was that gas flow rates could be determined at the outlet, by measuring a gas volume change (ml) in the burette over a set change in time. The disadvantages of this method were that the flow rates could not be recorded continuously. Also, gas bubbles flow through the water column would disturb the water-gas interface and made liquid levels hard to read. Ultimately, Option (a) was chosen

since the continuous measurements easier to read on a continuous basis, which were necessary for the mass balance.

Data necessary to calculate relative permeabilities included: total fluid injected, pressure drop along the core, produced gas, and produced water (Johnson et al., 1957). Gas flow rates were measure in and out of the core using the flow transducers and water production was measured on a digital balance that communicated data directly to LabVIEW via serial port. Inlet, outlet, and differential pressures were automatically recorded and output to a text file every 4 seconds. Prior to data collection the transducers were calibrated to determine the proper conversion between voltage and pressure. Examples of calibration curves are included in Figure 4.7. Each curve was obtained by attaching a voltmeter to the transducer and measuring pressure with a digital pressure gauge. The slope of the trendline was input to the LabVIEW code to convert the voltage signal into pressure readings. Transducer 0 represents an example of poor calibration with some drift in the readings for different trials. Fortunately Transducer 0 is redundant with two others (2 and 4) to measure inlet pressures. Transducer 2 was very well-behaved and exhibited consistent results for several trials of calibration.

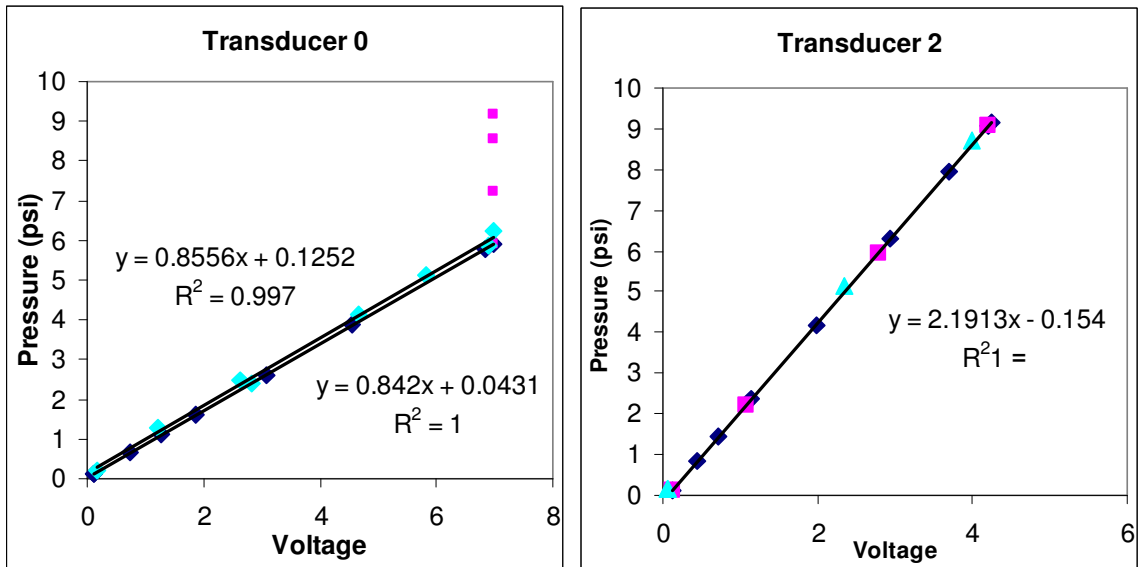


Figure 4.7 Calibration curves: transducer 0 shows poor calibration at high pressures, whereas transducer 2 is a very well-behaved transducer.

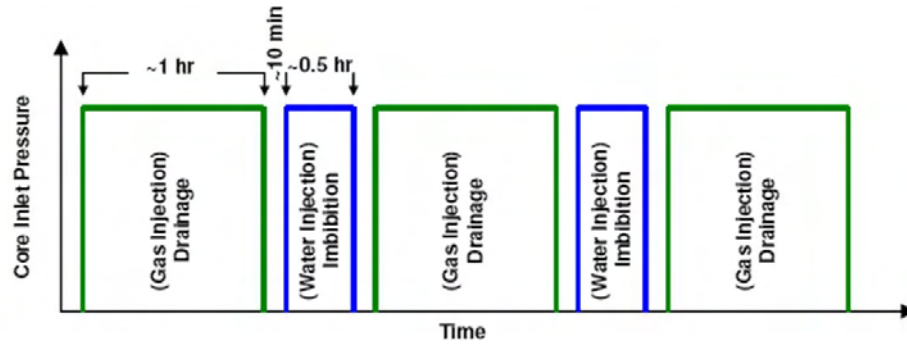


Figure 4.8 Schematic of injection schedule (from Stacey, 2008).

During each flow experiment, the inlet was held at a constant pressure of 4 psi for the duration of the drainage and imbibition experiments; the pressure was supplied by the gas canister and controlled with a pressure regulator. Outlet pressure was to atmosphere. A schematic of an experiment timeline is included in Figure 4.8.

The specific steps for each experiment are outlined as follows:

1. Saturate water with CO<sub>2</sub>: degas a container of distilled water (~ 1 hr), then saturate degassed water with CO<sub>2</sub>. Inject from the bottom of the water vessel, and then adjust the inlet pressure regulator to hold pressure inside the canister constant at about 5 psi for another hour.
2. Displace deaerated water with CO<sub>2</sub>-saturated water (175-200 ml).
3. Drainage: Inject gas until negligible fluid exits core (about 1 hr).
  - a. Record pressure (LabVIEW)
  - b. Record mass out (LabVIEW)
  - c. Record volumetric flow rate in and out (manually with stopwatch).
4. Rest core 10 minutes and switch the system to the imbibition setup.
5. Imbibition: Inject water until negligible gas exits core (20-30 min).

- a. Record pressure (LabVIEW)
  - b. Record mass out (LabVIEW)
  - c. Record volumetric flow rate in and out (manually with stopwatch).
6. Repeat. Previous work performed three cycles of drainage (Stacey, 2008), the experiment may be improved if the number of cycles was increased (see Section 4.2.4).

To switch the system from a CO<sub>2</sub> experiment to a N<sub>2</sub> experiment, or to restart an experiment, the following steps were followed:

7. Degas a container of distilled water (~ 1 hr).
8. Close all valves on the front of the transducer box<sup>1</sup>.
9. flow air through the core to drain water.
10. Vacuum the core to remove residual water:
  - a. I would vacuum from the outlet and bleed air from the inlet to drain residual water into the vacuum trap<sup>2</sup>.
  - b. When negligible water is exiting system, close air bleed and wait for vacuum pressure to drop below 100 millitorr.
11. Close valve to vacuum, release pressure in deaerated water vessel to atmospheric, and open valve to water vessel so that fluid saturates core and associated tubing.

---

<sup>1</sup> It was assumed that liquid water did not drain from lines behind the valves, so they were closed to avoid attaching the extra tubing to equalize pressure across transducers.

<sup>2</sup> As step 7.b is performed, watch the vacuum trap. Water will freeze in trap and may block the tube, in which case the trap must be thawed and drained before continuing.

12. Allow the core to equilibrate overnight (~ 12 hr).
13. Before running the next experiment, pressurize core and bleed vent lines on valves on front of transducer box.
14. Conduct N<sub>2</sub> drainage and imbibition experiment by repeating steps 1-6.

# Chapter 5

## 5. Core-Scale Experiment: Results

Core experiments were performed with the procedures detailed in Chapter 4. Experimental results and data analysis techniques are included in this chapter. First an explanation of preliminary pressure data is included, followed by data used for the JBN method and simulation results to model relative permeability.

### 5.1. JBN Method

A later trial provided the following data set that was used to calculate relative permeabilities using the JBN method (Section 5.2) and history matching (Section 5.3). All of the pressure transducers began to behave poorly immediately after the first drainage phase (Figure 5.3). Figure 5.4 displays a chart of the “corrected” pressure data set, which was generated by assuming a constant pressure drop of about 2 psi and subtracting this  $dP$  from the inlet pressure (Transducer 2 was the only one that seemed to be providing reasonable data). No apparent changes to the system were made, the transducers were unpressurized, and so the reason for the deviation is not clear.

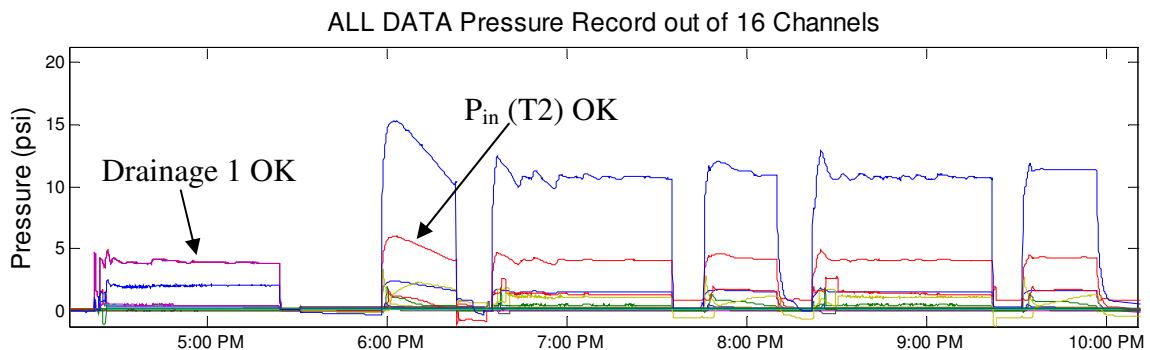


Figure 5.1 Raw data from transducers. First cycle is OK; all remaining transducers except for Transducer 2 are not.

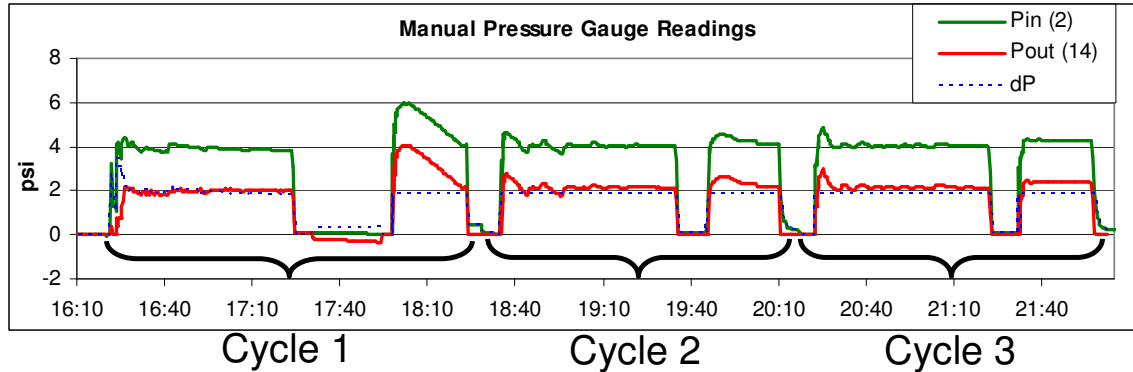


Figure 5.2 “Corrected” pressure data; assumes a constant  $dP$ .

Production data are included in Figures 5.5 – 5.6. These data were used to calculate relative permeabilities in accordance with Buckley-Leverett theory as outlined in Appendix A. Because the cumulative gas injection is so great (11 – 14 liters) The difference between the gas in and out is not visible. It should be noted that the higher resolution flow rate meter (8272) was used at the inlet. After completion of the experiment the measured flow (dashed lines) ended up nearly coincident with the calculated gas production line (Figure 5.6). Total water production declines with each cycle of drainage and imbibition. This makes sense because the first drainage is of a water-saturated core where the largest volume of water may be displaced. After the first imbibition, water is returned to the pore space, but not to complete saturation due to the immobile gas phase. Based upon totals of fluid injected and produced a mass balance was maintained to calculate residual water saturations.

Table 5.5 Calculations of residual water saturation based upon mass balance:

|             | Drainage 1  |       | Imbibition 1 |       | Drainage 2  |       | Imbibition 2 |       | Drainage 3  |       | Imbibition 3 |       |
|-------------|-------------|-------|--------------|-------|-------------|-------|--------------|-------|-------------|-------|--------------|-------|
|             | Water       | CO2   | Water        | CO2   | Water       | CO2   | Water        | CO2   | Water       | CO2   | Water        | CO2   |
| Initial Vol | 128.50      | 0.00  | 50.76        | 77.74 | 115.37      | 13.13 | 48.31        | 80.19 | 104.01      | 24.49 | 45.75        | 82.75 |
| injected    | 0.00        |       | 234.30       |       | 0.00        |       | 170.40       |       | 0.00        |       | 170.40       |       |
| removed     | 77.74       |       | 169.69       |       | 67.06       |       | 114.70       |       | 58.26       |       | 115.23       |       |
| Final Vol   | 50.76       | 77.74 | 115.37       | 13.13 | 48.31       | 80.19 | 104.01       | 24.49 | 45.75       | 82.75 | 100.92       | 27.58 |
| S           | <b>0.40</b> | 0.60  | 0.90         | 0.10  | <b>0.38</b> | 0.62  | 0.81         | 0.19  | <b>0.36</b> | 0.64  | 0.79         | 0.21  |

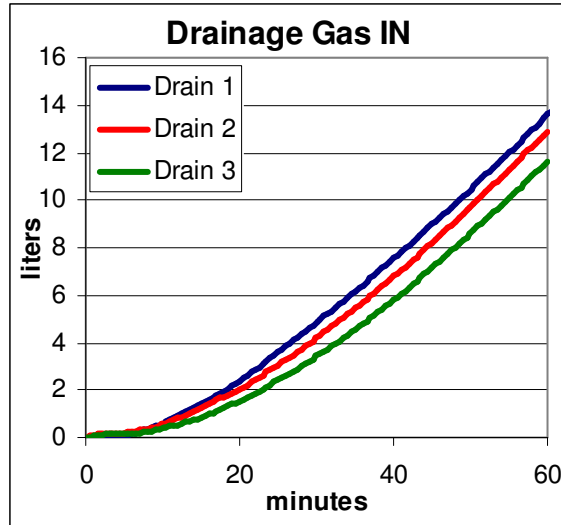


Figure 5.3 Cumulative gas injection volume; legend applies to Figure 5.6 too.

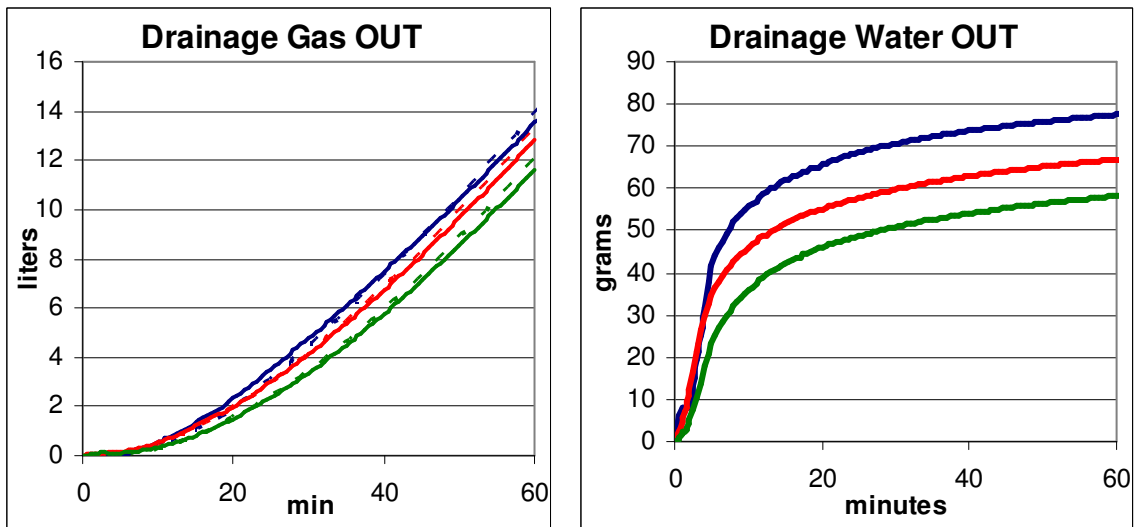


Figure 5.4 Cumulative production curves: (a) Cumulative gas production; solid lines are calculated values and dashed lines were measured values, (b) Cumulative water production.

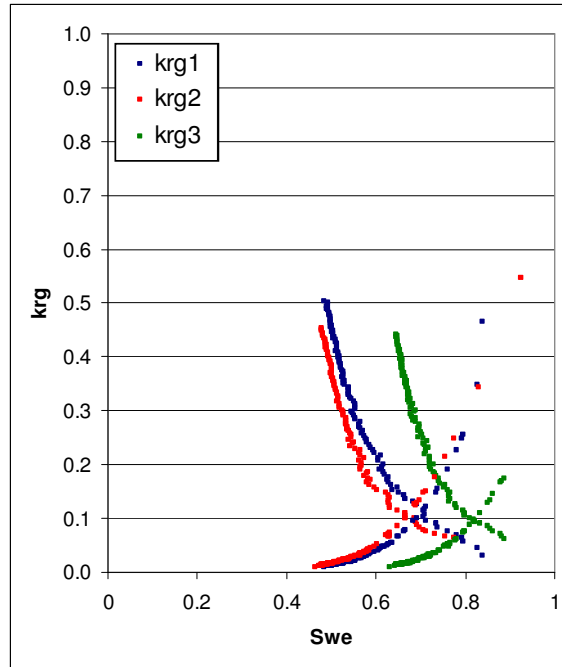


Figure 5.5 Relative permeability curves for drainage 1, 2, and 3.

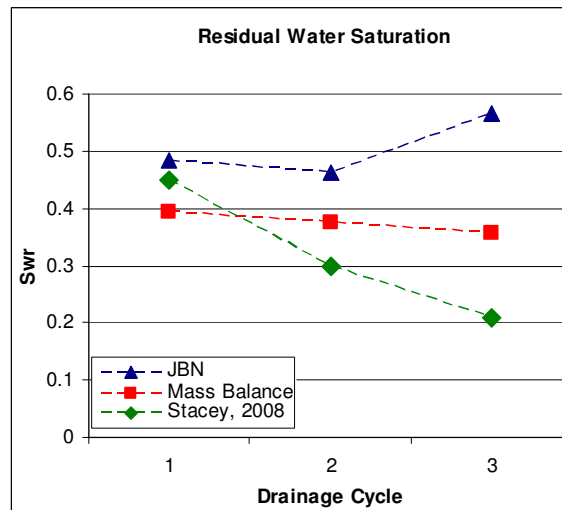


Figure 5.6 Residual water saturation over time.

Residual gas saturations calculated with the JBN method do not match the mass balance values (Figure 5.8). I suspect this may be because some water mass continued to be produced during the breaks between cycles. The JBN method cannot account for this mass because there are no gas flow rates registered during the breaks. So for the mass balance the mass production during the breaks was accounted for, whereas in JBN calculations it was not. This results in lower residual water saturation  $S_{wr}$  for the mass

balance calculations because more water was removed. Drainage 3 provides puzzling results. When calculating the residual saturation from the mass balance the trend of decreasing  $S_{wr}$  continues, however the relative permeability curves calculated from the JBN method are much higher and inconsistent with the previous two cycles. It was not possible to conclude if this was a result of a calculation mistake. Regardless, the first and second cycles of drainage result in a decreasing residual water saturation and the third drainage cycle data is inconclusive. All residual water saturation values are within a range comparable to data previously reported by Stacey (2008).

## **5.2. Improvements to System**

Some improvements to the experimental configuration and methods are noted.

1. The laboratory experiments will likely benefit by modifying to a vertical core holder. Previous studies have shown by X-ray tomography that the gravity effect is quite significant and CO<sub>2</sub> often rose to the top of core and resulted in a low sweep efficiency (Perrin et al., 2009 and Egermann, 2006). Displacement from the top of a vertical column appeared to reduce the gravity effect. For the current system, rotating the core holder would involve a major overhaul that would include either changing the orientation of the transducer box, because the core holder and box are connected by metal tubing, or redoing the connections between core holder and transducers.
2. The total inlet fluid may have been measured using another balance. However, with the current setup the mass of the water-filled canister and stand exceeded the 6 kg capacity of the laboratory scales. A higher-capacity scale or modified (lighter) equipment would solve this.
3. More than three cycles of drainage and imbibition should be conducted. The protocol should perhaps be modified to continue drainage and imbibition cycles until residual water saturation stabilized.

4. It also may be possible to set up a Matlab code, Excel macro, or PetraSim project to check relative permeabilities and/or saturations during breaks between cycles to check on the status of the core.
5. It would be useful to implement the capillary end effect correction scheme reported by Bennion and Thomas (1991); summarized in Appendix A.

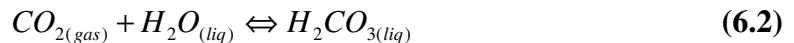
# Chapter 6

## 6. Theoretical Studies

Some theoretical studies were undertaken to try to determine if the active phase change (APC) behavior would be present at higher temperatures and pressures. This was conducted by first looking at CO<sub>2</sub> solubility (Section 6.1) and then diffusion rates (Section 6.2).

### 6.1. Solubility Model

In order to calculate diffusion rates, it is necessary first to determine initial concentrations via CO<sub>2</sub> solubilities. CO<sub>2</sub> solubility in water is quite complex because it is dependent on a variety of conditions including temperature, pressure, and salinity (Konrad and Bird, 1995). A CO<sub>2</sub>-water system seeks to achieve equilibrium between the following equations:



At atmospheric conditions the rate of Equation 5.2 is quite slow with only about 10-5 m (i.e. mol H<sub>2</sub>CO<sub>3(aq)</sub> per kg water) at equilibrium while the rest of the CO<sub>2</sub> remains as CO<sub>2(aq)</sub> (Konrad and Bird, 1995).

Experimental data from Dodds et al. (1956) were used to draw a set of smooth curves as their best interpretation of the isobaric solubility versus temperature (reproduced here as Figure 6.1, left). The Duan Group's model was used to generate a similar figure based upon their CO<sub>2</sub> equation of state (Figure 6.1, right). The theoretical data (Figure 6.1, right) seems to match the experimental data quite well. These data give us confidence to

trust the model's predictions for higher temperatures and pressures where experimental data is not available.

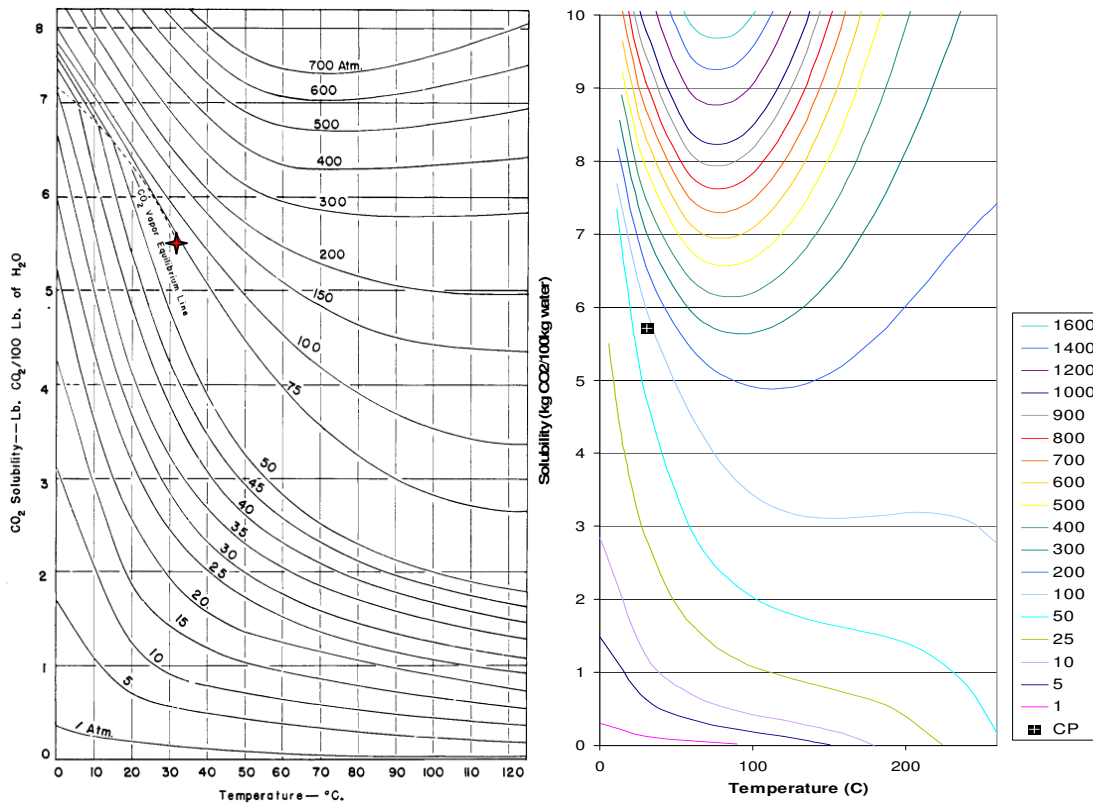


Figure 6.1 (Left) Experimental data versus (Right) Data from thermodynamic model.

From these data, it is clear that solubility is highly sensitive to changes in pressure and temperature. Both experimental and theoretical data show that, at any given temperature, increasing pressure will universally increase solubility. Temperature is less straightforward. At low temperatures (generally less than 100°C), a decrease in temperature raises CO<sub>2</sub> solubility. At higher temperatures solubility seems to be less sensitive to temperature changes. Above about 200 atm and 100°C, the model shows that a temperature increase leads to an increase in solubility (Figure 6.1).

So, for higher pressure, low temperature reservoirs, higher concentrations may be expected thus the effect of active phase change may be expected to be greater. Current understanding of a viable EGS source would require a high pressure, high temperature.

Under these conditions CO<sub>2</sub> would be supercritical and CO<sub>2</sub> solubility is predicted to be high. For example a 200°C reservoir at 500 atm would have a calculated solubility of about 10 kg CO<sub>2</sub>/100 kg water, or about 10% of fluid mass.

Other parameters affect the solubility of CO<sub>2</sub> in water. Salinity was shown to decrease CO<sub>2</sub> solubility. Introduction of a basic solution would neutralize the weak acid, H<sub>2</sub>CO<sub>3</sub>, forcing Equation (5.2) to the right allowing more CO<sub>2</sub> (gas) to dissolve into solution (Konrad and Bird, 1995). Similarly, if the partial pressure of CO<sub>2</sub> (gas) were to be increased the forward reaction would be favored and more CO<sub>2</sub> would dissolve.

## 6.2. Diffusion Rate Study

A simple one-dimensional diffusion model was generated to simulate diffusion of CO<sub>2</sub> through water, where concentration in the water ( $C$ ) was calculated as a function of position ( $x$ ) and time ( $t$ ) given the general 1-D diffusion equation (Crank, 1975):

$$\frac{\partial C(x,t)}{\partial t} = -D \frac{\partial^2 C(x,t)}{\partial x^2} \quad (6.3)$$

The interface was assumed stationary with a constant concentration boundary; all boundary conditions were defined as:

$$C(x = 0, t) = C_o \quad (6.4)$$

$$C(x > 0, t = 0) = 0 \quad (6.5)$$

$$C(x \rightarrow \infty, t) = 0 \quad (6.6)$$



Figure 6.2 Schematic of semi-infinite slab diffusion model.

Given the boundary conditions (Equations 6.4 – 6.6), Kreft and Zuber (1978) presented a full solution to the diffusion equation using the complimentary error function:

$$C = C_o \left\{ \frac{1}{2} \operatorname{erfc} \left( \frac{x-Ut}{\sqrt{4Dt}} \right) + \frac{1}{2} \exp \left( \frac{Ux}{D} \right) \operatorname{erfc} \left( \frac{x+Ut}{\sqrt{4Dt}} \right) \right\} \quad (6.7)$$

As we assumed a stationary boundary, the velocity terms ( $U = 0$ ) disappear and the equation simplifies to:

$$C = C_o \left\{ \operatorname{erfc} \left( \frac{x}{\sqrt{4Dt}} \right) \right\} \quad (6.8)$$

A diffusion coefficient ( $D$ ) was selected based upon experimental and modeled diffusivities reported in Tamimi et al, 1994, values ranged from  $1.60 \times 10^{-5}$  to  $1.76 \times 10^{-5}$   $\text{cm}^2/\text{s}$  at atmospheric temperature ( $20^\circ\text{C}$ ). A diffusion coefficient of  $D = 1.70 \times 10^{-3}$   $\text{mm}^2/\text{s}$  in units applicable to the pore scale range. Model results show a normalized concentration that gives a sense of relative rate of concentration increase versus distance (Figure 6.3). A Berea sandstone pore throat length is on the order of  $100 \mu\text{m}$ . Looking at the right chart (Figure 6.3) it looks like the concentration at the end of the pore throat would reach  $C_o/2$  in about 7 sec and would reach  $3/4 C_o$  in about 30 sec.

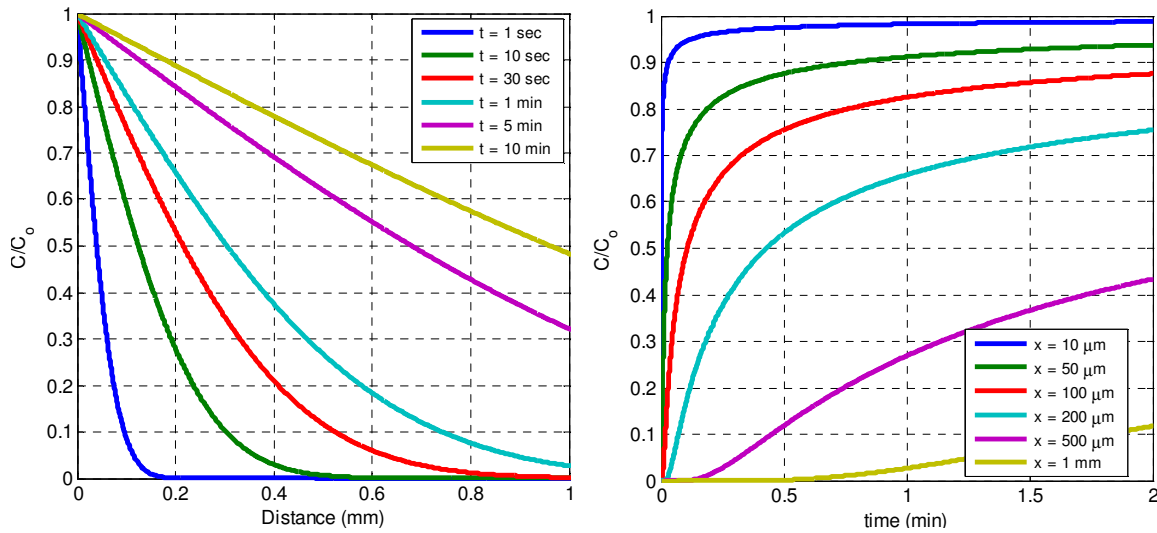


Figure 6.3 Diffusion model results: (left) normalized concentration versus distance for lines of constant time, and (right) normalized concentration versus time for lines of constant distance.

Previous work indicated a maximum injection velocity of about 8.5 cm/min, which corresponds to about 1.4 mm/sec. The speed at which the front moves through the core under the current conditions is orders of magnitude higher than the rate of concentration increase as a result of diffusion. For example, about  $\frac{1}{2} C_o$  would reach 1 mm after 10 min. As noted above the time-scale is on order of tens of seconds for shorter lengths (50-100  $\mu\text{m}$ ), which is reasonable for the pore scale. As such, it appears that at high injection rates diffusion may not be immediately relevant to the advancing gas-liquid interface, but may be relevant to the immobile water that remains after drainage.



# Chapter 7

## 7. Closing

### 7.1. Conclusions

Previous work had identified a phenomenon called “active phase change” (APC) that was considered significant when evaluating the two-phase flow behavior of CO<sub>2</sub> and water. This project focused on determining repeatability of previous work, and establishing a detailed experimental procedure that could be followed in the future. The micromodel work indicated that mass transfer was occurring by the observed dissolution of CO<sub>2</sub> bubbles and the growth and shrinkage of CO<sub>2</sub> bubbles while disconnected within the pore space.

The core-scale experimental results provided data that could be used with the JBN method to calculate relative permeabilities and indicate that the residual water saturation was decreasing over time. However, the last drainage cycle was inconclusive and disrupted the decreasing trend of residual water saturation  $S_{wr}$ . In contrast to the JBN results,  $S_{wr}$  data calculated from the mass balance did continue its decreasing trend over all three drainage cycles. The reason for this discrepancy is not clear at this time, but may be related to the fact that the mass balance includes water production data over the break period, which appear resulted in a larger volume of water removed, thus lower  $S_{wr}$ .

In addition, some theoretical work was conducted to predict relative importance of APC varied conditions of temperature, pressure, or salinity. From the exercise it was clear that the solubility of CO<sub>2</sub> in water is highly sensitive to changes in temperature or pressure. At low temperatures, CO<sub>2</sub> increases in the solubility, but at higher temperatures (above about 100°C) Pressure becomes the more dominant variable where an increase in pressure basically universally generates a solubility increase. In addition, the diffusion model presented in Section 6.2 illustrated the time and length scales that may be relevant for

APC. For APC to have a significant effect on flow behavior, diffusion would be required to occur fast enough so that supersaturation can occur in order for bubble nucleation and dissolution. The simple one-dimensional diffusion model seemed to indicate that diffusion and bubble nucleation may not be relevant in the flow behavior of the advancing front, but it does have the potential to interact with immobile water that would be left behind after drainage.

The implications of these findings are significant to potential plans to inject CO<sub>2</sub> into the subsurface. In the context of CO<sub>2</sub> sequestration, knowledge of APC behavior may help optimize injection schemes so that a greater volume of CO<sub>2</sub> may be stored underground. For example, cycling injection with periods of low pressure to allow CO<sub>2</sub> to come out of solution and remove additional immobile water over time, as was observed in the core experiments, may provide a greater percentage of pore space available to CO<sub>2</sub> than would have been otherwise predicted. In addition, the diffusion of CO<sub>2</sub> in water means that CO<sub>2</sub> may enter the smallest pore spaces without overcoming capillary pressure. Therefore, water may remain trapped either in solution, or by forcing residual water out of the small pore spaces, such as the conceptual model illustrated and described in Section 2.2.

In addition, for CO<sub>2</sub> EGS, a primary concern is how quickly the reservoir will be stripped of its connate water so that corrosive effects of hydrochloric acid may be avoided. Similar to a CO<sub>2</sub> sequestration injection scheme, it is possible for CO<sub>2</sub> to enter the smallest pore spaces that it would not be able to enter assuming pure hydrodynamic forces. The by cyclically pausing injection, lowering the pressure, and continuing injection, it may be possible to lower the residual water saturation more quickly than by maintaining a constant injection rate.

## **7.2. Recommendations for Future Work**

It is recommended that work on this project continues to define the constraints of APC and its effect under various experimental conditions, considering variables such as: gas, salinity, flow rate, pressure, temperature, or rock type. Care should be taken to change only one variable at a time. There is limited work that has been reported about unsteady-

state relative permeability experiments, which was summarized in Chapter 2. The issue with a lot of this work is the differing experimental setups, methods, and data collection techniques make comparison between datasets difficult or meaningless. I propose the following recommendations for future experimental setups in conjunction with the guidelines that were outlined in Section 4.2.2 and suggested in Section 5.4:

- A vertical core setup would eliminate gravity effect and improve core sweep efficiency
- X-ray tomography would be helpful to observe core heterogeneity or determine saturation profiles
- More than three cycles of drainage and imbibition should be conducted. Cycles should be continued until the residual water saturation stabilizes at a constant values. An automated program (LabVIEW, Excel, or Matlab) may be helpful to calculate saturations or relative permeabilities during breaks between phases. In addition, Bennion and Thomas (1991) present a simple method to determine if capillarity is significant and to correct end point relative permeabilities if necessary.

Aside from the experimental methods, it would be informative to repeat both the micromodel and the core experiments at higher pressures and temperatures to see if a similar behavior is observed. One concern with the higher temperatures may be chemical alteration of the core, corrosion, or mineral precipitation. It is easier to control pressure, so it may be advisable to first investigate the effect of pressure before modifying the temperature of the experiment.

A pore network model seems like it would be a natural extension to this work. Li and Yortsos (1999) used a pore network simulation to look at bubble nucleation and growth in micromodels. Chalbaud et al. (2007) also generated a pore network model to match relative permeabilities and residual gas saturation.



## Nomenclature

*APC* = active phase change

*CCS* = carbon capture and sequestration

*Drainage* = gas injection

*EGS* = Engineered Geothermal System

*Imbibition* = water injection

*JBN* = Johnson, Baussler, and Naumann



## References

- Bennion, D.B, and Bachu, S., 2008, "Drainage and Imbibition Relative Permeability Relationships for Supercritical CO<sub>2</sub>/Brine and H<sub>2</sub>S/Brine Systems in Intergranular Sandstone, Carbonate, Shale, Anhydrite Rocks," SPE Reservoir Evaluation & Engineering, 11(3), 487-496
- Brown, D.W., 2000, "A Hot Dry Rock Geothermal Energy Concept Utilizing Supercritical CO<sub>2</sub> Instead of Water," Proceedings 25th Workshop on Geothermal Reservoir Engineering, Stanford University, 233-238.
- Buchgraber, Markus, 2011, "A Micromodel Investigation of Gas Trapping," SUPRI-A Annual Meeting
- Chalbaud, C., Lombard, J.-M., Martin, F., and Robin, M., 2007, "Two Phase Flow Properties of Brine-CO<sub>2</sub> Systems in Carbonate Core: Influence of Wettability on P<sub>c</sub> and k<sub>r</sub>," SPE/EAGE Reservoir Characterization and Simulation Conference, Abu Dhabi, U.A.E., October 28-31
- Chang, Y., Coats, B.K., and Nolen, J.S., 1998, "A Compositional Model for CO<sub>2</sub> Floods Including CO<sub>2</sub> Solubility in Water," Society of Petroleum Engineers, 155-160.
- Chen, CY (2005), "Liquid-Gas Relative Permeabilities in Fractures: Effects of Flow Structures, Phase Transformation and Surface Roughness," PhD thesis, Stanford University.
- Crank, N., 1975, *The Mathematics of Diffusion*, Oxford University Press, Oxford, England
- Dodds, W.S., Stutzman, L.F., and Sollami, B.J., 1956, "Carbon Dioxide Solubility in Water," Industrial and Engineering Chemistry, Vol. 1, No. 1, 92-95.

- Dria, D.E., Pope, G.A., and Sepehrnoori, K., 1993, "Three-Phase Gas/Oil/Brine Relative Permeabilities Measured Under CO<sub>2</sub> Flooding Conditions," SPE Reservoir Engineering, Vol. 20184, 143-150
- Duan, Z., and Sun, R., (2003), "An Improved Model Calculating CO<sub>2</sub> Solubility in Pure Water and Aqueous NaCl Solutions from 273 to 533 K and from 0 to 2000 bar," Chemical Geology, 193, 257-271.
- Duan, Z., Sun, R., Zhu, C., and Chou, I, (2006), "An Improved Model for the Calculation of CO<sub>2</sub> Solubility in aqueous Solutions Containing Na<sup>+</sup>, K<sup>+</sup>, Ca<sup>2+</sup>, Mg<sup>2+</sup>, Cl<sup>-</sup>, and SO<sub>4</sub><sup>2-</sup>," Marine Chemistry, 98, 131-139.
- Engel, T., and Reid, P., 1996, *Thermodynamics, Statistical Thermodynamics, and Kinetics*, Pearson, Benjamin Cummings, San Francisco, CA
- Johnson, E.F., Bossler, D.P., and Naumann, V.O., 1957, "Calculation of Relative Permeability from Displacement Experiments
- Juanes, R., Spiteri, E.J., Orr Jr., F.M., and Blunt, M.J., 2006, "Impact of Relative Permeability Hysteresis on Geological CO<sub>2</sub> Storage," Water Resources Research, Vol. 42, W12418
- Konrad, B.K. and Bird, D.K. (1995), Introduction to Geochemistry, Third Edition, McGraw-Hill, Inc., New York, NY.
- Kreft, A., and Zuber, A., 1991, "On the physical meaning of the dispersion equation and its solutions for different initial and boundary conditions," Chemical Engineering Science, Vol 33, 1471-1480
- Li, X. and Yortsos, Y.C., 1995, "Visualization and Simulation of Bubble Growth in Pore Networks," American Institute of Chemical Engineers, Col. 41, No.2, 214-222
- Li, X. and Yortsos, Y.C., 1995, "Visualization and Simulation of Bubble Growth in Pore Networks," American Institute of Chemical Engineers, Col. 41, No.2, 214-222

- Müller, N., 2011, “Supercritical CO<sub>2</sub>-Brine Relative Permeability Experiments in Reservoir Rocks—Literature Review and Recommendations,” *Transport in Porous Media*, Vol. 87, 367-383
- Perrin, J.-C., Krause, M., and Benson, S.M., 2008, “Relative Permeability Properties of the CO<sub>2</sub>/Brine System in Saline Aquifers: An Experimental Study,” *Seventh Annual Conference on Carbon Capture & Sequestration*, Pittsburgh, p. 22
- Perrin, J.-C., Krause, M., Kuo, C.-W., Miljkovic, L., Charoba, E., and Benson, S.M., 2009, “Core-Scale Experimental Study of Relative Permeability Properties of CO<sub>2</sub> and Brine in Reservoir Rocks,” *Energy Procedia*, Vol. 1, 3512-3522
- PetraSim 5, *User Manual*, Thunderhead Engineering, Manhattan, KS
- Potter, R. M.; Robinson, E. S. and M. C. Smith, 1974, “Method of Extracting Heat from Dry Geothermal Reservoirs,” U.S. Patent #3,786,858
- Pruess, K. (2006), “EGS using CO<sub>2</sub> as Working Fluid – A Novel Approach for Generation Renewable Energy with Simultaneous Sequestration of Carbon” *Geothermics*, 35, 351-367.
- Pruess, K., Oldenburg, C., and Moridis, G., 1999, “TOUGH2 User’s Guide, Version 2.0,” Earth Sciences Division, Lawrence Berkeley National Laboratory, U.C. Berkeley, CA
- Randolph, J.B. and Saar, M.O. (2010), “Coupling Geothermal Energy Capture with Carbon Dioxide Sequestration in Naturally Permeable, Porous Geologic Formations: A Comparison with Enhanced Geothermal Systems,” *GRC Transactions*.
- Stacey, R., 2008, “The Impact of Dynamic Dissolution on Carbon Dioxide Sequestration in Aquifers,” *Engineer Thesis*, Stanford University
- Stacey, R., Pistone, S., and Horne, R.N., 2010, “CO<sub>2</sub> as an EGS Working Fluid – The Effects of Dynamic Dissolution on CO<sub>2</sub>-Water Multiphase Flow,” *GRC Transactions*

- Stacey, R., Pistone, S., and Horne, R.N., 2011, "The Significance of CO<sub>2</sub> Solubility in Geothermal Reservoirs," Proceedings 36<sup>th</sup> Stanford Geothermal Workshop
- Tamimi, A., Rinker, E.B., and Sandall, O.C., 1994, "Diffusion Coefficients for Hydrogen Sulfide, Carbon Dioxide, and Nitrous Oxide in Water over the Temperature Range 293-368 K," Journal of Chemical Engineering Data, Vol. 39, 330-332
- Tsimpanogiannis, I.N. and Yortsos, Y.C., 2002, "Model for the Gas Evolution in a Porous Medium Driven by Solute Diffusion," Environmental and Energy Engineering, Vol. 48, No. 11, 2690-2710

# Appendix A

## A. Buckley-Leverett Theory

The JBN method is commonly used to calculate relative permeabilities from unsteady-state core flood experiments using the water and gas production histories (Johnson et al, 1959). The JBN method was derived from Buckley-Leverett flow theory, therefore the method has several inherent assumptions (Bennion and Thomas, 1991):

1. No capillary pressure or capillary end effects
2. No gravitational effects
3. Calculation is only applicable during spreading-wave portion of flow saturation profile, e.g. after gas breakthrough in a drainage experiment.
4. Homogenous rock, and perfectly dispersed flow

The equations to calculate relative permeabilities from experimental data are summarized as follows, which have been modified to apply to the current CO<sub>2</sub>-water system (Bennion and Thomas, 1991 and Horne, 221 Course Notes):

- During drainage make a note of when gas breakthrough occurs. This was done visually by extending the outlet tubing into the Erlenmeyer flask separator so that bubbles could be observed in the water (see Figure 4.4). This gave an indication of when gas breakthrough occurred and when Buckley-Leverett theory may apply, to satisfy Assumption 3 above. Using this theory, fractional flow is defined as:

$$f_w = \frac{q_w}{q_w + q_g} \quad \text{and} \quad f_g = 1 - f_w \quad (\text{A.7.1})$$

- At any point along the core it is assumed that the flow is governed by the following modification to the Darcy equation for two-phase flow:

$$q_w = q_T f_w = \frac{k k_{rw}}{\mu_w} A \frac{\partial P}{\partial x} \quad (\text{A.7.2})$$

At the start of displacement water saturation is 1, no gas is flowing (i.e.  $k_{rg} = 0$ ), thus the total flow rate may be defined as:

$$q_T = q_w = \frac{kA}{\mu_w} \frac{\Delta P}{L} \quad (\text{A.7.3})$$

From this we can define a “intake capacity” as:

$$\left( \frac{q_T}{\Delta P} \right)_{init} = \frac{kA}{\mu_w L} \quad (\text{A.7.4})$$

Then, using the intake capacity we can define “relative injectivity” as follows, which is the ratio of the intake capacity during experiment to the initial intake capacity:

$$I_r = \frac{q_T / \Delta P}{\left( q_T / \Delta P \right)_{init}} = \frac{q_T}{\Delta P} \frac{\mu_w L}{kA} \quad (\text{A.7.5})$$

Time was nondimensionalized using the standard pore volumes injected ( $PVI = t_D$ ):

$$t_D = \frac{q_T t}{V_p} \quad (\text{A.7.6})$$

where, pore volume ( $V_p$ ) is defined as porosity times total core volume. The ratio of relative permeability and fractional flow at the core outlet can be found graphically by calculating the slope of the following relationship (see Figure A.1):

$$\frac{f_{we}}{k_{rw}} = \frac{d\left(\frac{1}{I_r t_D}\right)}{d\left(\frac{1}{t_D}\right)} \quad (\text{A.7.7})$$

Now everything is known to calculate the relative permeability for each phase:

$$k_{rw} = \frac{f_{we}}{d\left(\frac{1}{I_r t_D}\right)} \Bigg/ \frac{d\left(\frac{1}{t_D}\right)} \quad \text{and} \quad k_{rg} = \frac{f_{ge}}{1-f_{we}} \frac{\mu_g}{\mu_w} k_{rw} \quad (\text{A.7.8})$$

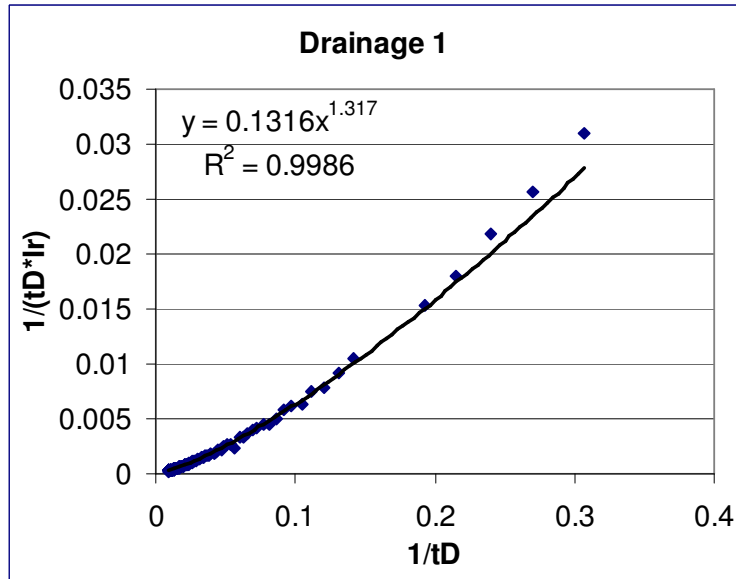


Figure A.1 Example plot for of  $1/(t_D \times I_r)$  vs.  $1/t_D$  for Equation A.11.

### A.1. End Effect Correction

In addition to the JBN method, history matching techniques using simulation software were also presented as a means to determine relative permeability curves (Section 2.1.1). Most simulators require endpoint permeabilities as input. Bennion and Thomas (1991) presented a simple correction technique to check the validity and correct the endpoint relative permeabilities for history-matching models.

Generally, end effects are a result of capillarity, where  $P_c = P_g - P_w$ , which may distort the calculated end point permeabilities. The method includes the following:

1. Conduct the general unsteady-state flow experiment as described in Section 4.2.2.
2. Use simulation technique to complete the relative permeability curves

3. Increase the flow rate of the displacing fluid for two to three additional higher flow rates.
4. Record any additional production of residual water saturation.

After completing these few extra steps there are three possible scenarios reported by Bennion and Thomas (1991):

1. Endpoint relative permeabilities do not change with increased flow rates, thus capillary end effects are deemed negligible.
2. Endpoint permeabilities increase with increased injection rates, which could be a result of capillary effects, a reduced residual water saturation or a combination of both.
3. Endpoint permeabilities decrease or behavior does not follow a consistent trend. This could be an indication of damage in core, fines mobilization, or turbulent flow. If it is suspected that turbulent flow had occurred the authors suggested repeating the experiment with lower injection rates to remain in the laminar flow regime. If fines have mobilized and reduced permeability the correction technique may still be applied as long as there are sufficient data points (three minimum).

The correction method uses a least-squares optimization routine to fit the data to the following nonlinear model by adjusting the constants  $a_1$  and  $a_2$ :

$$k_i = a_1(1 - \exp(-a_2 q_i)) \quad (\text{A.7.9})$$

Then,  $a_1$  is used to scale the original end permeability and the rest of the curve is normalized to the new value. See Bennion and Thomas (1991) for an example problem (Table 2).

This correction technique was not used for the experiment reported here, however it could be implemented easily in future trials.

# Appendix B

## B. LabVIEW Program

LabVIEW is a software package by National Instruments that was used to input data from the pressure transducers as well as the balance. Each transducer sends a voltage signal that is transmitted via one positive and one negative wire for each channel (Figure B.1). The system used for the current study uses a total of 16 channels (CH 0 through CH 15) from the 16 transducers, which are connected to the core apparatus as shown in Figure 4.3. The LabVIEW program uses “Virtual Instruments” (VIs) to control and/or read data from analogous physical instruments. The code for this project was developed by expanding LabVIEW’s “DAQ Assistant” express VI and modifying as outlined in Figure B.4, a screenshot of the front panel is displayed in Figure B.3.

To use the program LabVIEW must know how to connect to the channels that transmit data. If you are trying to set up LabVIEW and the data collection program on a new computer you will need to first mount the chassis and define which slot to read. This is all done through LabVIEW’s Measurement & Automation Explorer (Figure B.2).

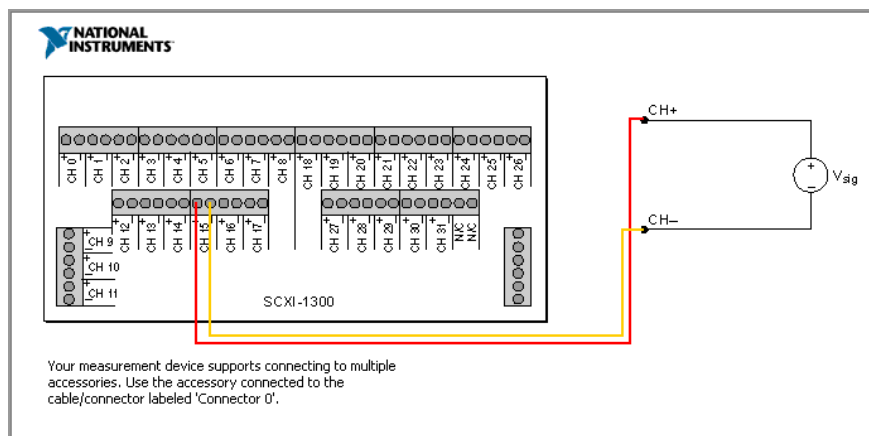


Figure B.1 Example diagram of SCXI connection

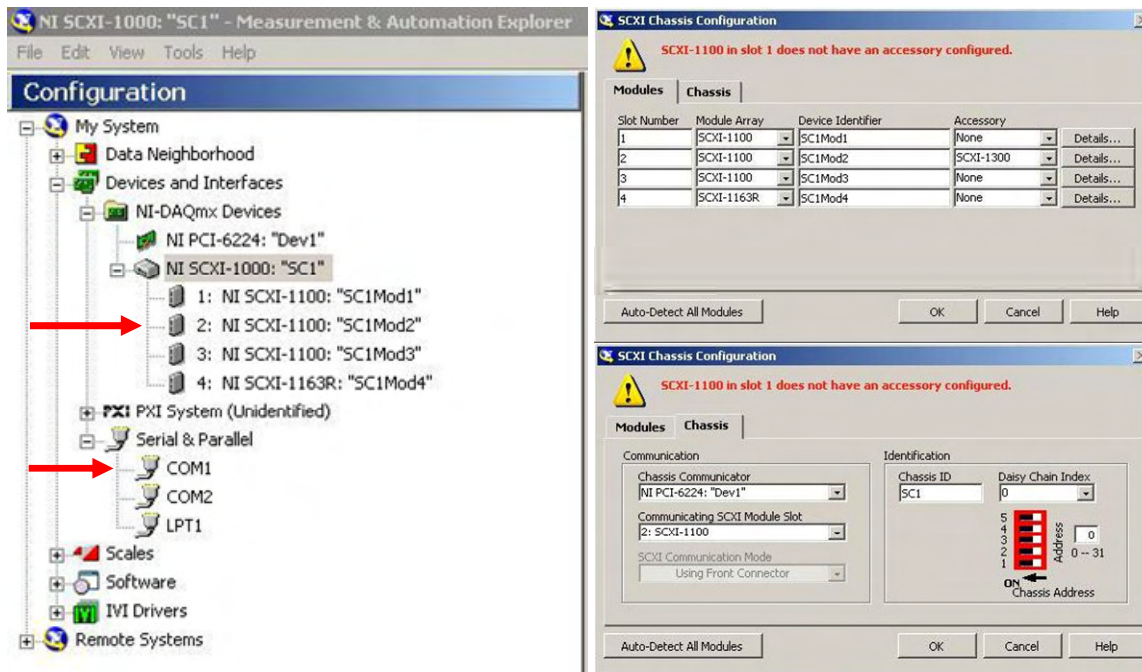


Figure B.2 Settings for chassis that transmits voltage data from pressure transducers.

For the current configuration we define the following:

Table B.1 Configuration for SCXI Chassis

|                       |              |
|-----------------------|--------------|
| Chassis communicator: | NI PCI-6224  |
| Device:               | NI SCXI-1000 |
| Slot:                 | 2            |
| Module:               | NI SCXI-1100 |
| Accessory:            | SCXI-1300    |

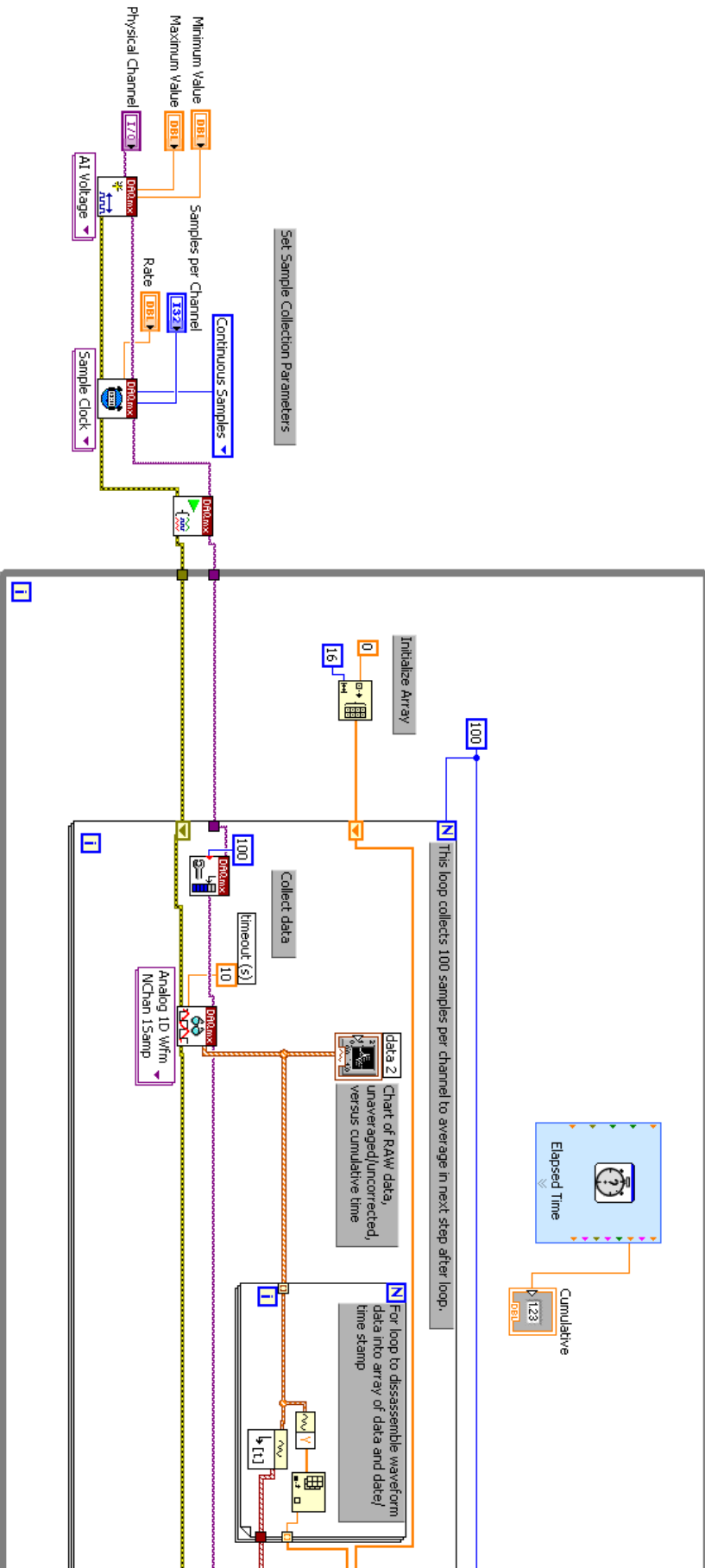
You can also open the Serial Port and test the connection to the balance from the Measurement & Automation Explorer (Figure B.2). Images of the front and back panels for the mass data collection program are included at the end of this appendix (Figures B.5–B.6). Parameters set within LabVIEW must match the output settings of the balance:

Table B.2 Balance model and settings

|                  |                |
|------------------|----------------|
| Brand:           | Mettler Toledo |
| Model:           | PB4002-S/FACT  |
| Peripheral unit: | Host           |
| Send format:     | SICS           |
| Send mode:       | S. Cont        |
| Baud rate:       | bd 9600        |
| Bit/Parity:      | 8b-no          |
| Handshake:       | HS Soft        |



The code below was created by expanding the 'DAQ Assistant' Express VI and modifying certain sections to collect and output data in the desired configuration. Double click on any icon to see corresponding feature on front panel. Press Ctrl+E to switch between front and back panels. Press Ctrl+H to show context help. Hover over any item to see brief description and link to full help file.



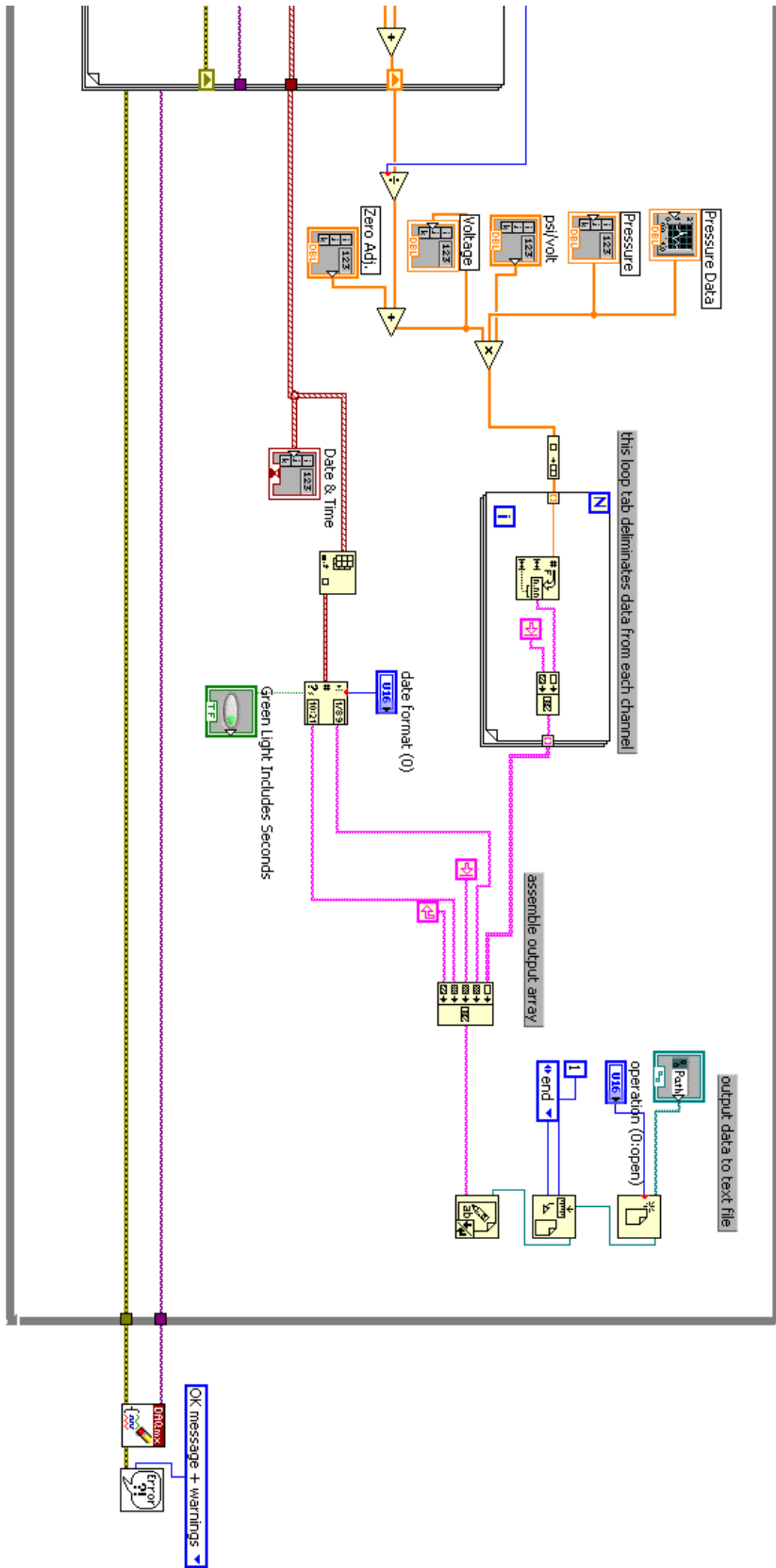


Figure B.4 Back Panel of LabVIEW code.

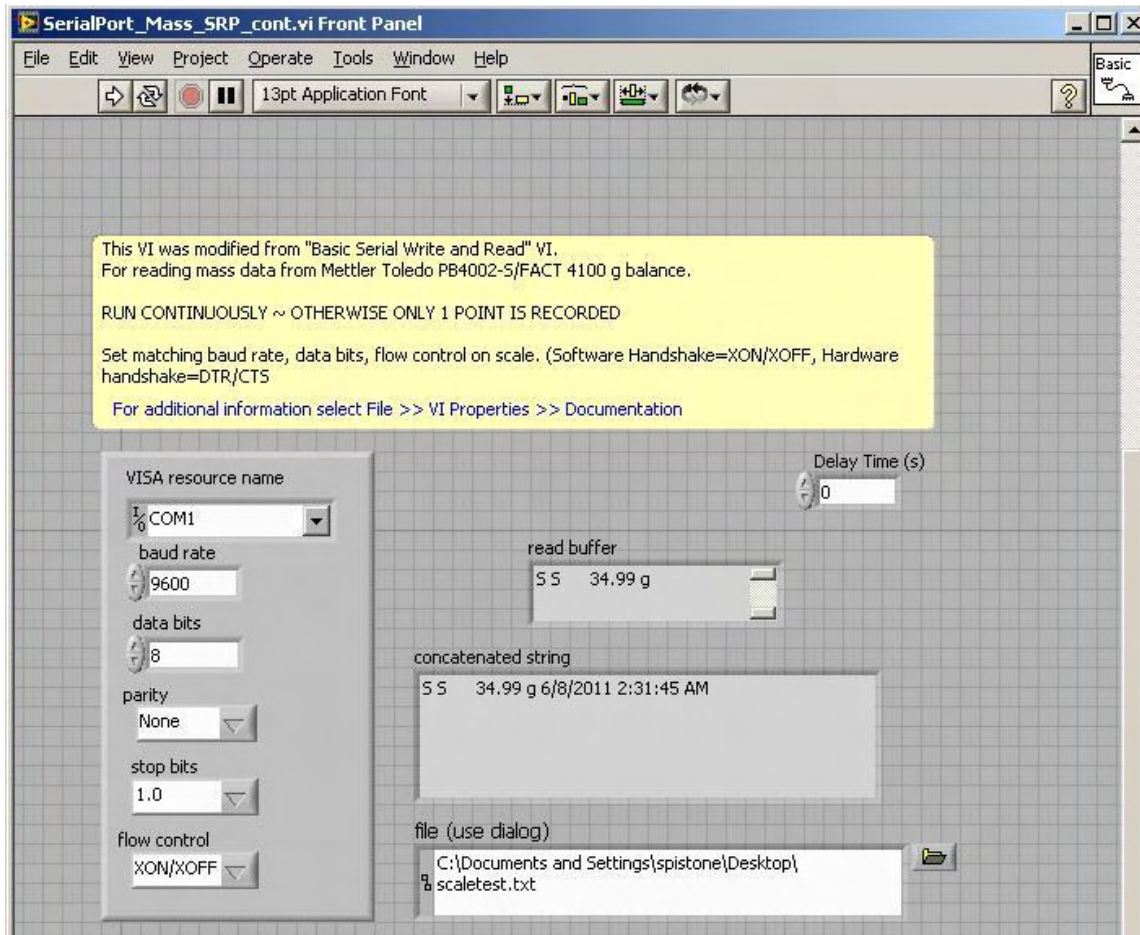


Figure B.5 Front panel of mass data collection program

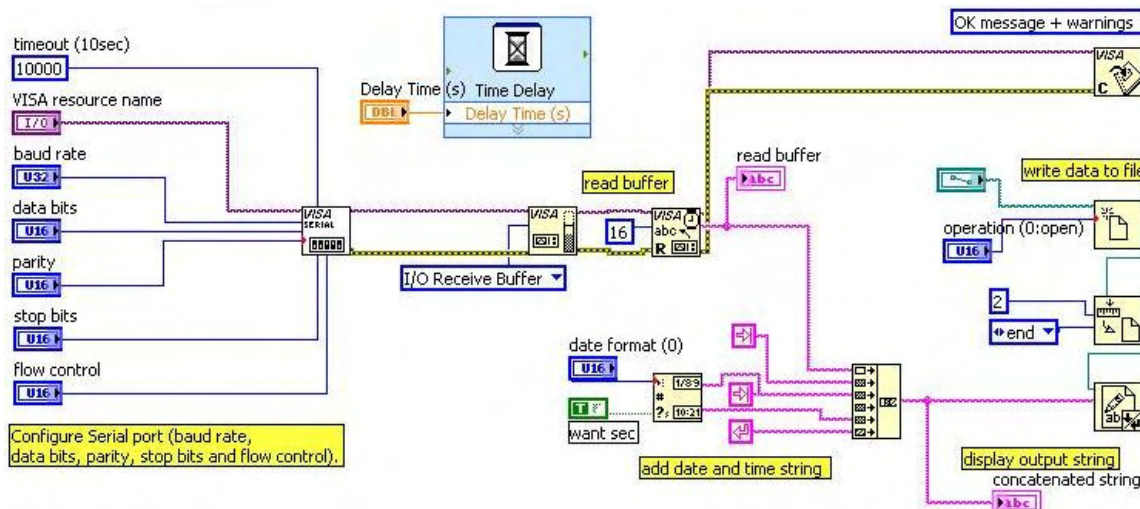


Figure B.6 Back panel of mass data collection program